SPIE.SPOTLIGHT

Experimental and Simulation Tools for Thin-Film Solar Cells

Carmen M Ruiz, David Duché, and Judikaël Le Rouzo

Experimental and Simulation Tools for Thin-Film Solar Cells

by Carmen M. Ruiz, David Duché, and Judikaël Le Rouzo

doi: http://dx.doi.org/10.1117/3.2244890
PDF ISBN: 9781510603660
epub ISBN: 9781510603677
mobi ISBN: 9781510603684

Published by

SPIE Press
P.O. Box 10
Bellingham, Washington 98227-0010 USA
Phone: +1 360.676.3290
Fax: +1 360.647.1445
Email: Books@spie.org
Web: http://spie.org

Spotlight vol. SL17
Last updated 15 July 2016

SPIE.

Table of Contents

Preface **v**

1 Introduction **1**

2 Materials and Solar Cells **2**

2.1 Generations of solar cells 2

2.2 Inorganic thin-film solar cells 3

2.3 Organic solar cells 5

2.4 Perovskite solar cells 7

3 Optical Experimental Techniques for Accurate Measurements **9**

3.1 Set of measurements for thin-film solar cells 9

3.1.1 Current–voltage curve analysis 10

3.1.2 Quantum efficiency 12

3.2 Ellipsometry 15

3.2.1 Optical modeling 15

3.2.2 Dispersion model 16

3.3 Photoluminescence 18

3.3.1 Excitonic transitions 19

3.3.2 Free-bound transitions 19

3.3.3 Donor–acceptor pairs 20

3.3.4 Band–band transitions 20

3.4 Photoreflectance 23

3.4.1 Photoreflectance on a $CuInS_2$ solar cell system 24

3.4.2 Combination of photoreflectance and photoluminescence for studying the bandgap of perovskite layers 25

4 Simulation Tools for Predicting Solar Cell Performances **26**

4.1 Optical modeling 26

4.1.1 Photonic crystals to trap the light in the active layer of organic solar cells 27

4.1.2 Color-tuned, highly efficient, organic solar cells 29

4.2 Optoelectronic simulation 30

4.2.1 Impact of the band alignment in a heterostructure: the CIG(SSe) system 32

4.2.2 Drift diffusion models for organic solar cells 34

5 Conclusion **37**

References **38**

SPIE Spotlight Series

Welcome to SPIE Spotlight eBooks! This series of tutorials is designed to educate readers about a wide range of topics in optics and photonics. I like to think that these books address subjects that are too broad for journal articles but too concise for textbooks. We hope you enjoy this eBook, and we encourage you to submit your ideas for future Spotlights online.

Robert D. Fiete, *Series Editor*
Harris Corp.

Editorial Board

Preface

This Spotlight describes the methods used for the optical characterization and design of thin-film solar cells. The cells under study include CdTe, CIGS, CZTS, perovskite, and organic solar cells. A description of these cells and the coupling of experimental and simulation studies is provided to improve the performances of thin-film solar cells. A detailed discussion of specific optical tools, such as ellipsometry, photoluminescence, and photoreflectance, is presented. The link between materials and measurements is made through the study of the physical principles involved in the functioning of these cells. Finally, the book details the numerical model that can be used to design the structure of a thin-film solar cell—a model in which the material properties have been extracted from the previous measurements, thus completing the design-characterization cycle.

1 Introduction

The potential of solar energy is now well established, yet photovoltaic technologies struggle to prevail in the energy landscape. There are problems with both the enhancement of the performances of the cells and the costs. In this context, thinning the different device layers is being envisaged in order to reduce the total costs of solar cells while maintaining their good performance. As the thicknesses of the different layers in a solar cell can be less than 100 nm in some cases, the importance of an optical design becomes critical for achieving competitive performances. Since photovoltaic solar cells are optoelectronic devices, mastering the interaction of light and matter is of utmost importance. Indeed, the behavior of the light in very thin-film layers is completely different than in bulk materials. Furthermore, even if the semiconductor materials used currently in the different technologies are quite good absorbers, the need for improved performances means that integrating photonic structures in the devices are increasingly envisaged. Thus, the photonic concepts must be considered as potential solutions to improve the photonic absorption of thin-film devices.[1]

The development of thin-film solar cells requires controlling the light inside the cell. Such control is not only useful to increase the efficiency but also for designing new kinds of solar cells such as "transparent and colored solar cells," which is interesting for building integrated photovoltaics. In these thin-film solar cells, the apparent color and the transparency are given by their reflected and transmitted spectra, taking into account human eye sensitivity. One can also use the light-management concept, i.e., using Bragg mirrors,[2] diffraction gratings,[3] surface plasmonic effects,[4] or photonic crystals[5] to optimize the cell performances.

The investigations into the improvement of solar cell efficiencies have also led researchers to look for new materials with optimized bandgaps that can absorb a large part of the solar spectrum. The mechanical flexibility, the low specific weight, and the color properties of these emerging materials open wide fields of applications. The optimization of the morphological and/or optical and/or electrical properties of these materials is thus a crucial issue today, along with the environmental and geopolitical issues (scarcity of elements, toxicity of elements, imported materials). It is obvious that all of the studies and progress have been and will be made keeping in view the final application. The applications are numerous—ground or building integration, mobile applications, and so on—and suggest that each technology can meet a given problem i.e., cost, efficiency, flexibility, color, and so on.

The new solar cell architecture is thus relatively complex and requires a thorough understanding of the materials' behavior, involving accurate knowledge of the electrical, optical, and structural properties of these materials. This Spotlight focuses on optical tools, both experimental and simulation, to improve the optical design of the thin-film solar cells. This approach provides a correct prediction and validation of device performance. Obviously, this work, directly related to the fields of optics and photonics, also involves the use of a more

comprehensive set of tools that includes structural (e.g., electronic microscopy, x-ray scattering, x-ray photoelectron spectroscopy, ultraviolet photoelectron spectroscopy, and atomic force microscopy) or electrical techniques (e.g., conductance measurements, Hall effect, and deep-level transient spectroscopy), which also contribute to the improved elaboration of the solar cells. Some of these techniques, although not described in this book, will be mentioned as related to our studies on solar cells.

2 Materials and Solar Cells

2.1 Generations of solar cells

Today, there are many types of solar cell technologies that use either organic or inorganic materials, or both. Research of photovoltaic solar cells is booming, not only on hybrid solar cells and thin-layer cells, but also on the new perovskite solar cells. Figure 1 illustrates the conversion efficiency of the best research solar cells worldwide, published by National Renewable Energy Laboratory (NREL; see Fig. 1), which can be compared with today's performance ranking chart. In this context, new materials for photovoltaics have emerged in recent years (inorganic nanostructures, organic materials, kesterites, perovskites, transparent conducting oxides, and so on) to increase cell performance while reducing technological costs.

Classical photovoltaic technology relies on the p-n semiconductor junction; the silicon solar cell is the example of what has been called first-generation photovoltaics. This technology, based on the preeminent silicon microelectronics technology, is at present the most industrialized and the most commonly used photovoltaic technology in the world. Nevertheless, a number of limitations prevent it from reaching the status of a really low-cost technology, such as the large amount of Si material needed for complete absorption of the incident light, the indirect bandgap, and the competition over this material with the more successful microelectronics market.

To overcome these problems, the second generation of photovoltaics proposed using materials with high absorption coefficients, allowing thin-film configurations and thus reduced use of materials. Mention may be made first of CdTe, CIGS (copper-indium-gallium-sulfide), kesterites (CZTS or copper-zinc-tin-sulfide), and GaAs, which are all direct bandgap materials, and second of amorphous silicon and microcrystalline silicon (indirect bandgap). CdTe, CIGS, and CZTS photovoltaic materials are deposited in the form of polycrystalline thin films. CdTe, CIGS, and CZTS photovoltaic devices are deposited as a polycrystalline thin film, offering very competitive manufacturing costs but limited efficiencies due to a high defect density. Silicon thin films are based on hydrogenated amorphous and hydrogenated microcrystalline silicon (a-Si:H, μc-Si:H), which are usually deposited by plasma-enhanced chemical vapor deposition. The best efficiency for this technology is obtained with a triple junction.[6] Epitaxial GaAs solar cells, on the other hand, can have very high efficiencies,

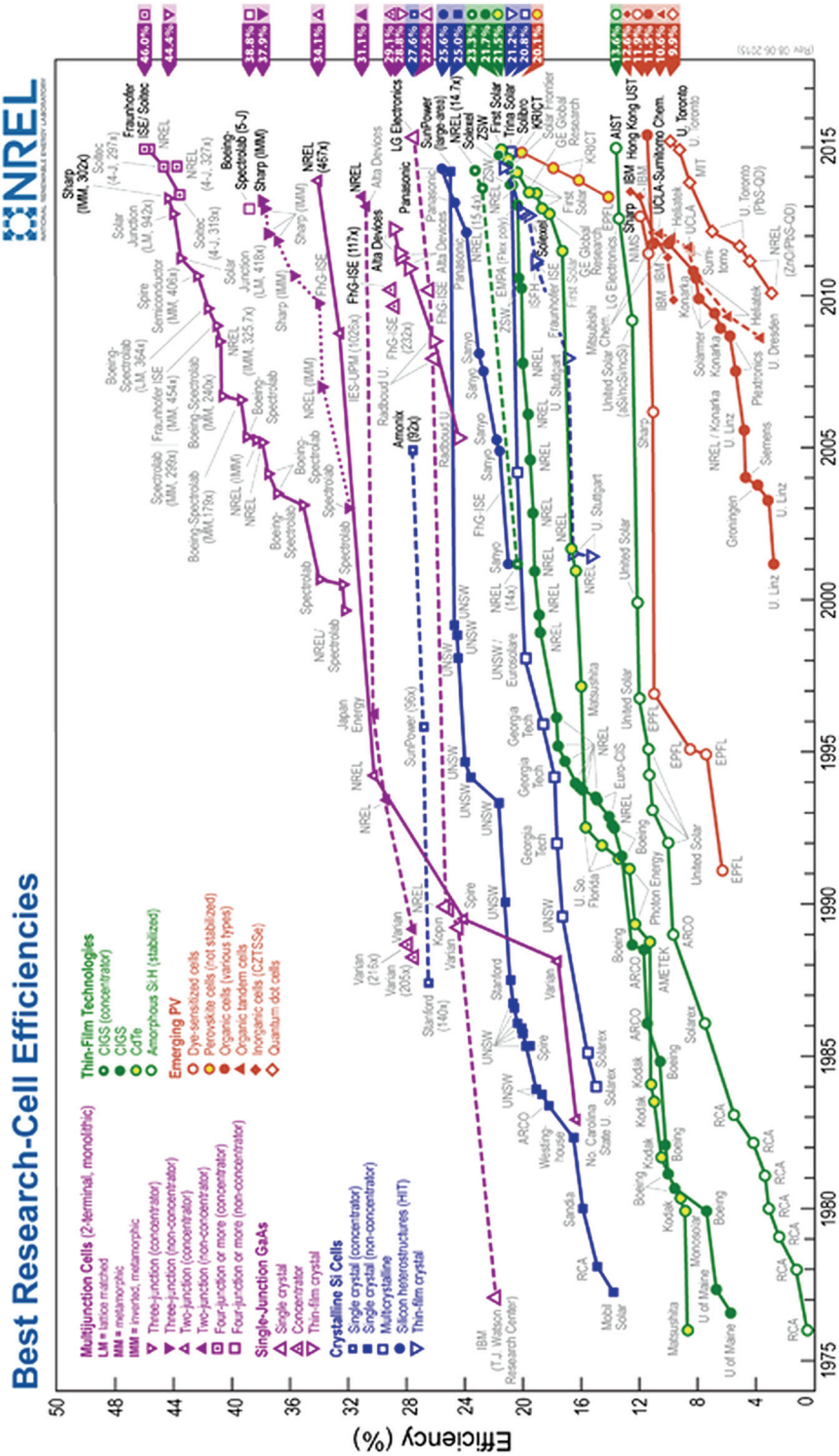

Figure 1 Conversion efficiencies of best research solar cells worldwide for various photovoltaic technologies since 1976.
Source: NREL, Golden, CO—United States Department of Energy.

but the process of fabrication is very expensive, which effectively limits their industrial implementation.

Finally, third-generation photovoltaics is the latest family of solar-energy-harvesting devices, and it includes all of the new concepts that are beyond the pn junction, such as multijunction devices, intraband solar cells, hot carrier absorbers, or organic solar cells (OSCs). In this context, special attention is paid to the exploitation of the whole light spectrum, and alternative solutions are proposed out of the device configuration.

In this Spotlight, we will focus on the study of second- and third-generation thin-film solar cells, made of different materials such as CIGS, CZTS, CdTe, and perovskite, as well as semiconducting polymers. We will describe each material to understand their possible limitations. A cell is made up of a stack of thin layers, and each layer consists of a different material. The optical properties of the different materials are of great importance for the final performance of the cell. Perfect knowledge of these properties is based on a comprehensive set of very precise measurements. However, this is not enough, and models are necessary to define the final optical parameters of the new materials that make up the cell.

2.2 Inorganic thin-film solar cells

CIGS- and CdTe-based solar cells have reached more than 21% efficiency,[7] which shows the great potential of these technologies for applications that need high energy-conversion efficiency. The best efficiency of CZTS solar cells, which belong to a more recent technology, is around 12.6%.[8] CZTS has been studied in the context of a major deployment of solar energy, bearing in mind the limited resources of indium and gallium, the latter being used in CIGS solar cells.

Thanks to their high absorption coefficients, the absorbing layers in these three polycrystalline solar cells can be relatively thin (<1 μm to a few microns thick). They can be deposited on several foreign substrates, such as glass sheets, metal foils, or polyimide foils. These three technologies differ in the realization of the absorbed layer: congruent sublimation and post-treatment in the case of cadmium telluride, and phase transformation by selenization or sulfurization of metal precursors in the case of chalcopyrites [$CuIn_{1-x}Ga_x(Se_{1-y}S_y)_2$] and kesterites [$Cu_2ZnSn(Se_{1-x}S_x)_4$].

CdTe, CIGS, and CZTS belong to the semiconductor material families II–VI, I–III–VII and II–VI, respectively. The thin-film solar cells made of these materials can be realized either in a substrate configuration [illumination usually through a transparent conductive oxide (TCO)] or in a superstrate configuration (illumination through a transparent glass superstrate). These two configurations differ in the deposition sequence: from the substrate to the TCO for the substrate configuration, and from the glass superstrate to the metallic back contacts for the superstrate configuration (as shown in Fig. 2). In both cases, we need TCO to provide

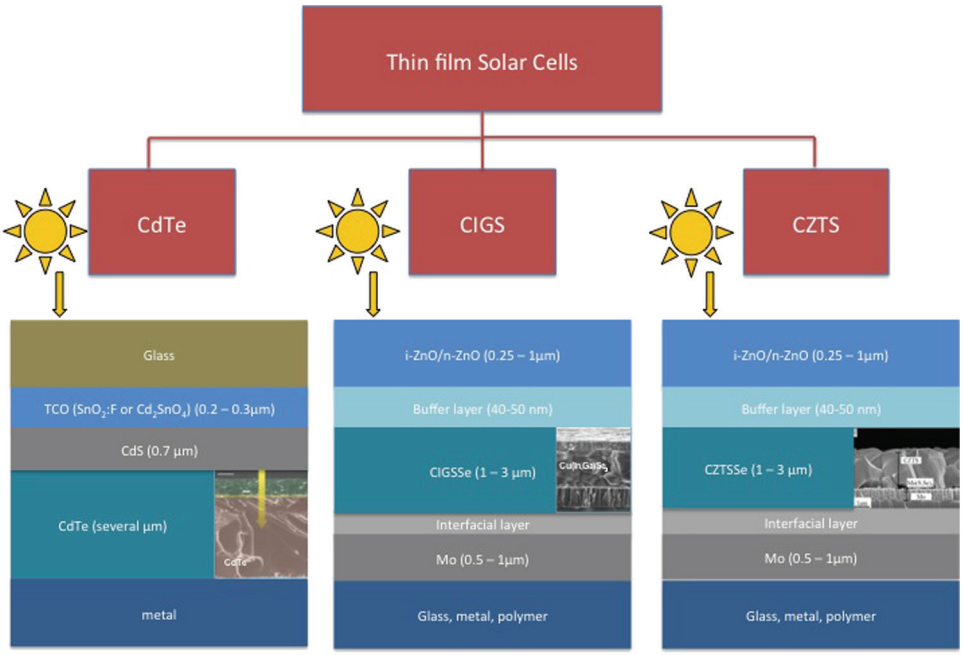

Figure 2 The typical structures of CdTe-, CIGS-, and CZTS-based thin-film solar cells. The SEM micrographs at the level of the absorber layer show the cross-section of the device. *Source*: CdTe[10] and CZTS.[8]

high transparency in the absorption range of the absorber and high conductivity. The role of these additional layers in a thin-film solar cell is of great importance, as we will see in Section 2.3. Figure 2 presents the typical structure of thin-film solar cells based on CdTe (superstrate configuration), CIGS (substrate configuration), and CZTS (substrate configuration). As we can see, these heterostructure solar cells propose a lot of different interfaces, even in the absorber layer. The grain boundaries in a polycrystalline absorber film can be considered as interfaces as well. It is thus a possible source of recombination, which has to be taken into account in the optoelectronic modeling of the device.

The bandgap of CdTe is around 1.5 eV. Depending on the stoichiometry of the chalcopyrite, the bandgap ranges from 1.04 and 1.68 eV for CIGS solar cells and from 1.0 to 1.5 eV for kesterite solar cells. These values are in the range of energy that allows high solar-energy conversion.[9]

2.3 Organic solar cells

OSCs are one of the most relevant photovoltaic technologies, as they are solution-phase processable and can be applied as thin-film coatings using imprint techniques such as roll-to-roll and ink jet. Thus, organic materials can be used to

reduce manufacturing costs. Furthermore, intense research on improving efficiency has led researchers to look for new materials with an optimized bandgap capable of absorbing a larger part of the solar spectrum.[11–13] Particular attention has been paid to the relative positions of lowest unoccupied molecular orbital (LUMO) and highest occupied molecular orbital (HOMO) levels with respect to the acceptor material. The HOMO and the LUMO bands correspond to the valence and the conduction band in inorganic materials, respectively. The mechanical flexibility, the low specific weight, and the color properties of these emerging materials open up wide fields of applications, such as power-generating bags, laptops, mobile phones, and applications related to fashion and architectural applications.

However, OSCs still exhibit quite low power-conversion efficiencies (PCEs): "Heliatek" announced a record-breaking 13% cell efficiency in 2016. This is mainly due to the low absorbance of organic semiconductors in the range of the solar spectrum and the necessity of using thicknesses that range between a few nanometers and a few hundred nanometers.

There are fundamental physical differences between organic and inorganic semiconductors. In inorganic semiconductors at room temperature (RT), the absorbed photons directly generate free charge carriers (electrons and holes) that can be harvested at their respective electrodes. In OSCs, the absorbed photons generate bound electron–hole pairs called excitons. The exciton binding energies range from 50 meV up to >1 eV. Then the excitons have to diffuse and reach an interface between a donor and an acceptor material in order to be dissociated into free charges. This additional process resulting in exciton dissociation completely changes the scale of the physical phenomena involved in OSCs. In crystalline and polycrystalline silicon, the electron diffusion length can reach up to 200 μm. In organic materials, both the exciton diffusion length and the charge carrier diffusion length are in the submicron range (10 to 20 nm for excitons and 100 to 200 nm for charge carriers). The impact of these low diffusion-length values is twofold. As can be seen in Fig. 3, the active layer in the OSC architecture is no thicker than 200 nm. In addition, this active layer must be composed of a disordered bulk heterojunction (BHJ), which is a blend of donor and acceptor materials, which allows the exciton dissociation probability to be enhanced. As in BHJs, not all of the interconnectivities between materials are perfect, and some dead ends may be present; this thickness is a tradeoff between good absorbance—which imposes thicker layers—and good charge extraction—which imposes thinner layers. Furthermore, improving the carrier mobility within the materials would permit thicker films.

In this context, the characterization of the morphological, optical, and electrical properties of the materials is crucial in improving OSC efficiencies. Furthermore, photonic concepts must be considered as potential solutions to increase the photonic absorption of such thin-film devices while controlling their apparent color and transparency.

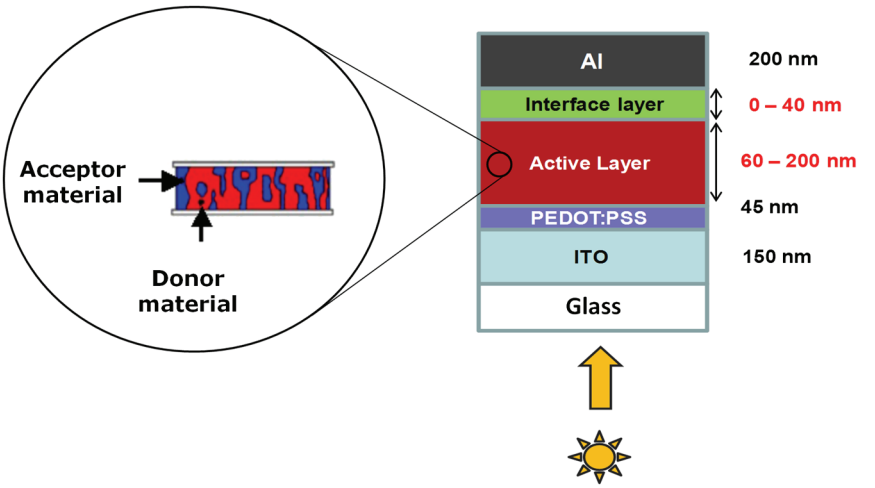

Figure 3 Schematic representation of a typical OSC architecture.

2.4 Perovskite solar cells

In recent years, the dye-sensitized solar cell (DSSC) technology has attracted a lot of attention. A DSCC solar cell is not based on the classical p–n configuration; in fact, its behavior mimics photosynthesis. A monolayer of a dye is deposited over a mesoporous oxide, which also works as a photoelectrode. A photon that arrives at the dye is absorbed, resulting in the excitation of an electron from HOMO to LUMO. The electrons are collected via the TCO. To regenerate the oxidized dye, an electrolyte solution containing a redox couple is used.[14] The efficiency of the best research cells is close to 12%, and some companies have started producing modules with reported efficiencies of 10.7%.[7] Through successive modifications, the liquid electrolyte has been replaced by a solid-state hole transporter, normally an organic semiconductor, with no significant impact on efficiency.[15]

In order to reduce the thickness of the whole DSSC cell, inorganic materials with high absorption coefficients started being used instead of organic dyes.[14] Although the performances were interesting (Sb_2S_3, 5%), this approach was not really a breakthrough until the application of organometallic halide perovskites, such as $CH_3NH_3PbI_3$ perovskite; DSCCs with perovskite nanocrystals exhibited 9.7% efficiency in 2012.[14–16] Soon after, the substitution of conducting TiO_2 by insulating Al_2O_3 in the mesoporous layer led to efficiencies of 10.9%, with a significant open-circuit voltage increment and no reduction of the short-circuit current.[15,17] This result provided evidence for the specific nature of these materials and suggested the possibility of using them in other configurations than DSCCs.

Organometal halide perovskites ABX_3 (A = alkyl-NH_3, B = Pb or Sn, X = I, Cl, or Br) represent a highly promising material thanks to their very sharp absorption features and their tunable bandgaps via chemical composition modification.

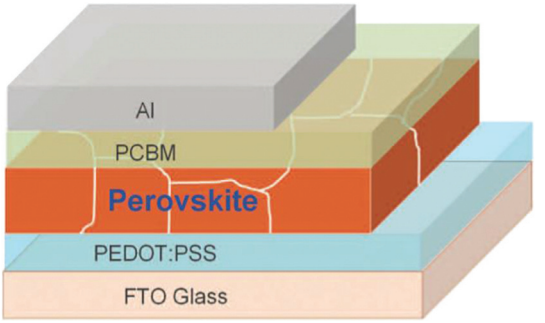

Figure 4 Planar device configuration for a perovskite solar cell. *Source*: Ref. 25.

For instance, these characteristics are of particular interest in the field of photovoltaic-integrated glass for windows, allowing the design of various devices with different transmittances or colors. Solar cells based on organometal halide perovskites have achieved PCEs as high as 20.1%[18] within a research time of merely 5 years.

Recent studies have shown that devices can be fabricated in a planar configuration (no mesoporous layer used)[19] or without a hole-transport layer, efficiencies being high enough (above 8%) to consider this material as the next step in photovoltaic technologies.[20]

Efficient perovskite-based solar cells have been prepared that have very different device structures—such as SSCs, hybrid organic or standard planar heterojunctions (cf. Fig. 4)—that all exhibit efficiencies reported to be over 10%.[21] Different bandgaps are also achievable by modifying the X-site composition (e.g., alloying iodine with bromine). Indeed, it is possible to change the bandgap of the semiconductor from 1.57 eV up to 2.3 eV[22] covering the visible spectrum up to the near-infrared. One can take advantage of this to design tandem solar cells that would allow a broader absorption of the light and higher efficiencies[15] and to adapt the transparency of the devices to selective ranges of the solar spectrum. In particular, it has already been reported that it is possible to fabricate semitransparent solar cells based on perovskite materials with efficiencies as high as 7% with an average transmittance of 30% in the visible range.[23,24]

Despite these amazing results, there is still a lot to learn about the behavior of perovskites in order to obtain maximum potential from these materials. For instance, the fact that no mesoporous layer is needed shows that perovskites can actually work like traditional semiconductors.[15,19,20] Furthermore, the analysis of the electrical properties, such as carrier density and mobility, points to a behavior more consistent with inorganic semiconductors than organic ones.[26,27] Nevertheless, there are still many questions to answer for obtaining a mature technology such as how the actual structure of the hybrid perovskite influences the

photovoltaic properties of the material,[15,28] if it is possible to substitute lead with less toxic elements such as Sn without too much efficiency loss,[15,29] and so on. One of the main limiting points at this moment for the evolution of these materials is their lack of stability. Their tendency to decompose under normal atmosphere can be a limiting factor in the fabrication of devices.

3 Optical Experimental Techniques for Accurate Measurements

3.1 Set of measurements for thin-film solar cells

This section presents the different optical techniques used for the advanced characterization of materials and cells. To develop accurate models that help us optimize the device design, we need knowledge of basic optical parameters such as the optical index or the dielectric permittivity. These parameters are linked with the absorption processes that lead to photogeneration and, as we know from thin-film solar cells, can vary strongly with the deposition method. Also, the range of absorption of the material will be an important parameter for the design of the tandem cells. All of these values can be obtained with a combination of spectroscopic ellipsometry (SE) measurements of the optical indices and spectrophotometric measurements of the R, T, and A (reflectance, transmittance, and absorption) spectra.

Generally, using the SE technique to determine optical constants of thin films requires knowledge of the optical constants of the substrate and measurements of the ellipsometric parameters ($\tan\Psi$ and $\cos\Delta$). Then the absorption (A) of the layer is predicted through modeling using optical indices (n and k) extracted from variable angle SE, and finally A is compared to the A deduced from reflectance (R) and transmittance (T) measurements. For thin-film solar cells, this is very challenging because of the anisotropy of the layer and/or the surface roughness. In addition, the application of such a method is hampered by a need for the accurate calibration of optical instruments. This could lead to important discrepancies between the measured absorption spectra and those predicted from the ellipsometric results assuming an isotropic model. To overcome these issues, detection of optical anisotropy can be achieved by measuring optical properties at varying incidence angles and by using an ellipsometer configuration providing the whole determination of the Mueller matrix coefficients. The influence of incorporation of the surface roughness correction can also be investigated using a Bruggeman effective medium approximation (EMA) to perform a surface roughness correction using a two-layer model, where the bottom layer is a blend film and the top layer is an EMA layer composed of air and bottom layer material. Due to the general difficulty of developing a comprehensive optical model for the new materials used today in photovoltaics, modeling of the assemblies is challenging but very rewarding in the end.

The combination of photoluminescence (PL) techniques with electroreflectance (ER) and/or photoreflectance (PR) can also be investigated for the analysis of the different layers in ultrathin devices, simultaneously determining their

fundamental and defect-related transitions. Low-temperature PL measurements can be performed with different excitation wavelengths for the analysis of optical confinements and other optical phenomena related to the back contact modification.

Even if this work is focused on optical measurements, we should not forget to discuss electrical measurements which lead to a better understanding of the whole behavior of a material or a cell. Electrical and optoelectronic characterizations of the devices involve their detailed analysis by measurements of the current–voltage at different temperatures of the internal quantum efficiency and of the external quantum efficiency. Detailed *I–V* measurements performed in the dark and under different illumination and temperature conditions are performed to achieve relevant information on the heterojunction band structure and to determine the main recombination mechanisms in the different cell architectures. This analysis could be combined with capacitance-based techniques such as capacitance–voltage as a function of the temperature [CV(T)] or drive level capacitance profiling, in order to analyze doping density, space charged region (SCR) size, defect distribution on the SCR and interface impact on the device.

3.1.1 Current–voltage curve analysis

Solar cell electrical behavior can generally be described as common diodes with an additional generated photocurrent. For the particular case of thin-film solar cells, the equation also has to take into account the effect of parasitic losses[30,31]

$$J = J_0 e^{\frac{q}{AKT}(V - JR_s)} + \frac{V}{R_{sh}} - J_{sc}, \tag{1}$$

where J_0 is the dark current, A is the diode ideality factor, R_s and R_{sh} are the series and shunt parasitic resistances, respectively, and J_{sc} is the photogenerated current.

In general, the diode ideality factor for thin solid films is found to be between 1.3 and 2, indicating that the main mechanism occurring in these devices is the trap-mediated recombination in the absorber.

The dark current J_0 can also be expressed as

$$J_o = J_{oo} e^{-\frac{\Phi_b}{AKT}}, \tag{2}$$

where J_{00} is a prefactor that takes into account the recombination mechanisms that control J_0 in forward bias, and Φ_b is the barrier height. If we take into account the two previous equations, we can express the open-circuit voltage, V_{oc}, as follows:

$$V_{oc} = \frac{\Phi_b}{q} - \frac{AKT}{q} \ln\left(\frac{J_{oo}}{J_{sc}}\right). \tag{3}$$

As the temperature tends to zero, the barrier height in these devices tends to the bandgap value, hence we obtain the maximum theoretical value for the

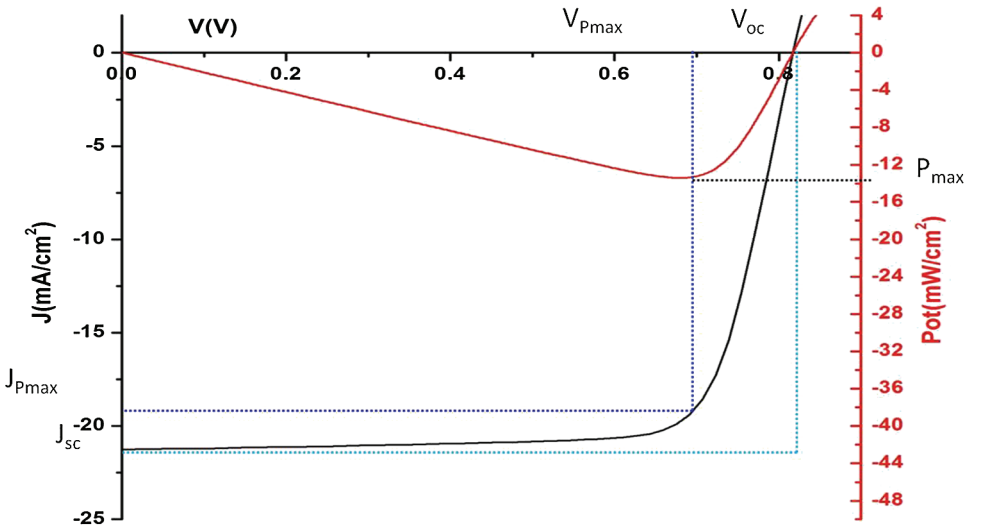

Figure 5 *JV* curve under illumination conditions for a CIGSe solar cell under illumination conditions. The most important parameters for analyzing the curve are identified.

open-circuit voltage. But as the temperature increases, the second term of the equation, which takes into account all the recombination mechanisms, becomes more and more important, which explains the main origin of the V_{oc} deficit of all these technologies.

In Fig. 5, the current–voltage curve for a CIGSe (copper-indium-gallium-selenide) solar cell under illumination conditions is represented. From this curve, it is possible to extract the main parameters that are used to evaluate the quality of a solar cell.

As previously defined, the open-circuit voltage, V_{oc}, corresponds to the voltage value at $J = 0$, where the curve intersects the voltage axis. Conversely, the short-circuit current, J_{sc}, corresponds to the point of the *JV* curve that intersects the *J*-axis. This J_{sc} has essentially the same value as the photogenerated current, and is, among all the parameters, the most directly related to the optical properties of the system. In most cases, it can be taken as constant with the voltage, but in some cases this is not true. We will analyze it in Section 3.1.2 dedicated to the quantum efficiency measurements.

Because a solar cell is an electrical power generator, we can define the maximum power delivered by the device by representing the product of the current and the voltage as a function of the voltage. This point is identified in Fig. 5 as $V_{P_{max}}$. In photovoltaics, the fill factor (FF) is defined as the ratio between the actual power obtained from a solar cell and the maximum power possible. It can be visually defined as the ratio between the area of the square formed by the current and voltage values corresponding to the maximum

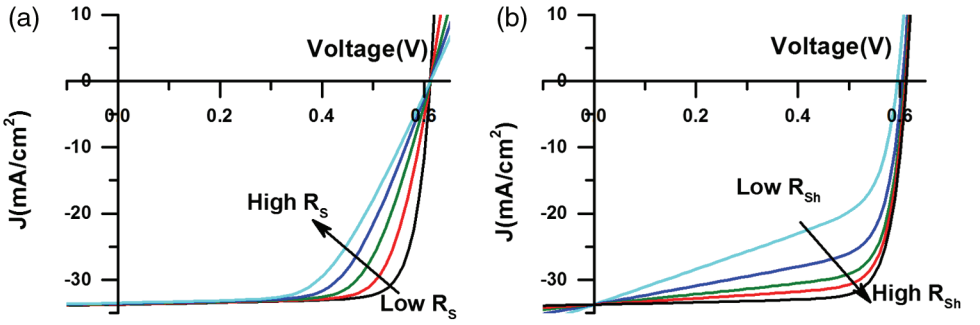

Figure 6 Impact on the *JV* curves of (a) increasing the series resistance and (b) decreasing the shunt resistance.

power (light blue in Fig. 5), and the area of the square formed by V_{oc} and J_{sc} (dark blue in Fig. 5)

$$\mathrm{FF} = \frac{J_{P_{max}} \cdot V_{P_{max}}}{J_{sc} \cdot V_{oc}} \cdot 100 = \frac{P_{real}}{P_{ideal}}. \tag{4}$$

The more ideal the behavior of a solar cell, the nearer the FF is to 100%. For the technologies considered in this Spotlight FF values are normally smaller than the ones obtained for silicon- and III–V-based solar cells, mainly because of the recombination processes that control the shape of the *JV* curve.

We can also define the efficiency (η), or the ratio between the electrical power extracted from the solar cell and the received irradiation power

$$\eta = \frac{P_{gen}}{P_{rec}} \cdot 100 = \frac{P_{max}}{P_{ilu}} \cdot 100 = \frac{\mathrm{FF} \cdot V_{oc} \cdot J_{sc}}{P_{ilu}} \cdot 100. \tag{5}$$

In order to standardize these measurements and to compare results from around the world, the efficiency should be measured with a spectrum equivalent in power (1000 W/m^2) and spectral shape to the one received from the sun at the surface of the Earth.

Parasitic resistance mainly affects the efficiency via the FF, as can be seen in Fig. 6.

3.1.2 Quantum efficiency

As previously noted, the photovoltaic parameter most closely related to the optical properties of the system is the short-circuit current, J_{sc}. By measuring the quantum efficiency, we obtain a measure of the current generated as a function of the wavelength. In this way, it is possible to determine the origin of the losses

in J_{sc}, by comparing with an optimal value. We can also write the J_{sc} of a solar cell as follows:[30,31,32]

$$J_{sc} = e \int_0^\infty S(E)QE(E)dE, \tag{6}$$

where $S(E)$ is the illumination spectrum as a function of the energy and QE is the quantum efficiency of the device. While the limits of integration here are 0 and infinity, in reality they are imposed by the bandgap of the materials in the solar cell. From this equation, it is straightforward that the higher the bandgap of a solar cell, the smaller the part of the spectrum that can be absorbed and thus the smaller the J_{sc}.

In Fig. 7, there is a quantum efficiency curve for an actual CIGSe-based solar cell as a function of the wavelength. We can see that the lower energy region of absorption is limited by the bandgap of the CIGSe—the perpendicular dotted line near 1150 nm in the figure. Also, it is clear that the device is far from the optimal absorption of the light in every wavelength. In the region where photogeneration is maximum, quantum efficiency is about 80%, indicating that almost 20% of the photons arriving with these particular energies are not used in the electron generation. Observing a quantum efficiency curve of a solar cell, we can have an idea of where these losses are produced and how we can optimize the device to improve current generation.

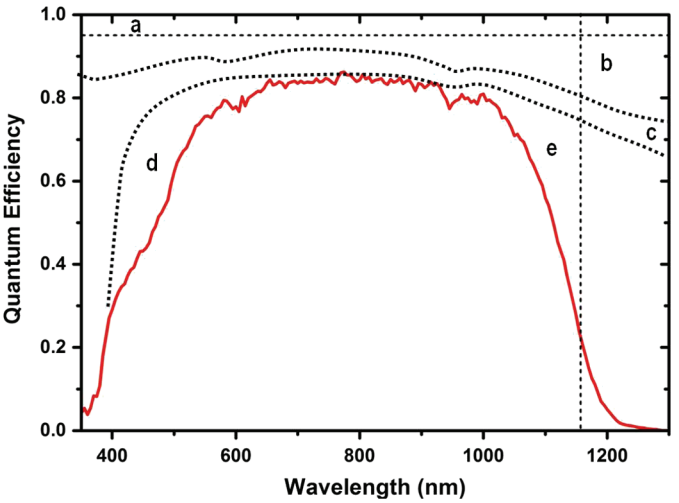

Figure 7 Quantum efficiency curve for a CIGSe solar cell with the main photogeneration losses identified.

In Fig. 7, different regions are identified, in which some photon or current loss mechanisms occur.[31,32]

(a) This region corresponds to the shadowing of the metallic collection grid in the front contact. The losses corresponding to this effect are uniform in the whole spectrum and correspond to 5% of the total incident light, i.e., the photocurrent proportional to the area covered by the grid. This loss can be improved by optimizing the grid design up to 2%.

(b) This part corresponds to the reflection at the interfaces of the front part of the solar cell. In particular for the case under study, the light has to pass the interfaces Air/ZnO/CdS/CIGSe, a small amount being lost on each reflection. This mechanism accounts for 8% to 10% of the total losses, and can be minimized by depositing an antireflection coating on the front side of the cell.

(c) There are also losses related to the absorption in the TCO layer. In the central region, the losses can be about 1% to 5%, depending on the thickness of the layer and its absorption [indium tin oxide (ITO) has a higher absorption coefficient than ZnO]. These values increase for $\lambda < 400$ nm, near the bandgap region of the TCO, and for $\lambda > 900$ nm, due to the absorption of light by the free carriers in the heavily doped TCOs.

(d) **Buffer layer absorption:** A typical buffer material is CdS, with a bandgap at 2.42 eV, and is responsible for the absorption of a vast part of the spectrum in the 500 nm region. These electron pairs generated in the buffer layer are not normally collected and do not contribute to the photogenerated current. To reduce this effect, two approaches are normally used: reduction in the thickness of the buffer layer, or substitution of the material by another with a higher bandgap. In the case of CIGSe, a lot of effort has been put into replacing the CdS, mainly with ZnS or In_2S_3, but the champion efficiency has been achieved with deposited CdS cells. Despite the light absorption due to its lower bandgap, the CdS/CIGSe band alignment is better than the ZnS/CIGSe one, contributing in other ways to a better performance of the cell.[33,34]

(e) **Losses in the absorber:** These losses can arise from an incomplete absorption of the light in the near bandgap regions, which can be solved by increasing the thickness of the absorber or by creating a back reflector via bandgap engineering. The other main origin of the losses in this region is the presence of recombination traps in the absorber. The lower energy photons, with a smaller absorption coefficient, are generally absorbed in the back of the absorber layer. If the diffusion length of the charges in the semiconductor is smaller than the distance they have to travel up to the SCR, the chances are that these charges are trapped and do not contribute to the photogeneration. In these cases, the photogeneration is going to be voltage dependent, because the SCR varies with the applied voltage, and the QE measured under applied reverse bias will be bigger than the one measured at equilibrium, this one being bigger than one measured under forward bias.[31]

3.2 Ellipsometry

SE is an efficient tool to determine the optical indices of bulk materials and materials in thin-film form. The optical indices can serve as input parameters to model the optical performances of thin-film solar cells, but are also of high interest for the extraction of information on the electronic properties of the materials.

SE is based on the change in polarization upon light reflection on a sample. The ratio between the Fresnel coefficients in p-polarization (r_p) and in s-polarization (r_s) allows extracting the amplitude and phase variations of the electric fields upon light reflection. It can be expressed as a function of the two ellipsometric angles (Ψ and Δ), as follows:

$$\frac{r_p}{r_s} = \tan \Psi e^{i\Delta}, \tag{7}$$

where $\tan(\Psi) = |r_p|/|r_s|$ represents the relative amplitude attenuation and $\Delta = \arg(r_p) - \arg(r_s)$ is the phase shift between the p- and s-polarizations. SE does not allow a direct determination of the optical indices of the materials. The first step consists of measuring the Ψ and Δ spectra of the sample and in a second step, a dispersion model is elaborated to determine the dielectric constant of the materials ($\varepsilon = \varepsilon_1 + i\varepsilon_2$). The dielectric constant determination consists of finding the adequate dispersion model which allows the Ψ and Δ spectra to be fitted through optical modeling. This process relies on the use of minimization algorithms to adjust the dispersion model parameters and the thicknesses of the layers. Then the wavelength-dependent optical indices n and k of the materials are obtained via the following equation:

$$\varepsilon = \varepsilon_1 + i\varepsilon_2 = (n + ik)^2. \tag{8}$$

3.2.1 Optical modeling

In the dispersion model elaboration, the calculated Ψ and Δ spectra have to be compared with the measured ones. A one-dimensional optical modeling such as the transfer matrix method (TMM) is usually used to calculate the Ψ and Δ spectra from the dispersion model. This is an elegant method allowing the modeling of the optical properties of flat thin films. Nevertheless, it implies that special attention should be dedicated to sample fabrication in order to obtain very flat layers. If the roughness of the layers is low in comparison with the wavelength of the incident light ($<\lambda/10$), a Bruggeman EMA can be implemented to perform a surface roughness correction. This is a major limitation for the determination of the optical indices for materials with much higher roughness.[35] Nowadays, in order to extend SE to nonplanar materials, research concerns the modeling of SE spectra using two-dimensional (2-D) and three-dimensional (3-D) optical simulation models such as the finite difference time domain (FDTD) model.[36,37]

3.2.2 Dispersion model

Several Kramer–Kronig consistent dispersion models can be used depending on the properties of the material studied. Cauchy or Sellmeyer functions are generally used for common dielectric materials such as ITO,[38] while Drude–Lorentz functions allow describing the optical properties of metals.[39]

Tauc–Lorentz models are adequate for the parameterization of amorphous thin films in the interband region.[40] It is especially useful for amorphous or semicrystalline materials, such as amorphous silicon and organic or hybrid organic/inorganic semiconducting materials, which exhibit bandgaps within the spectral range of the ellipsometer. Figures 8(a) and 8(b) show the optical indices n and k of hybrid organic/inorganic BHJs in P3HT:ZnO (1:2) and in PTB7:ZnO (1:2) obtained using Tauc–Lorentz models.[41] P3HT refers poly(3-hexylthiophene-2, 5-diyl), while PTB7 refers to poly[[4,8-bis[(2-ethylhexyl)oxy]benzo[1,2-b:4, 5-b0]dithiophene-2,6-diyl][3-fluoro-2-[(2-ethylhexyl)carbonyl]thieno[3,4-b]thiophenediyl]]. The correlation coefficients R^2 of the fits are 0.98 and 0.96 for P3HT:ZnO (1:2) and PTB7:ZnO (1:2), respectively. These values indicate appropriate fits to the data. Figures 8(c) and 8(d) show a comparison between experimental measurements and optical simulations of the reflection [$R(\lambda)$] and the transmission [$T(\lambda)$] spectra for P3HT:ZnO (1:2) and PTB7:ZnO (1:2) layers coated on glass. $T(\lambda)$ and $R(\lambda)$ spectra of the samples were measured with a CARY 5000 spectrophotometer from a Varian equipped with an integrating sphere. For the optical

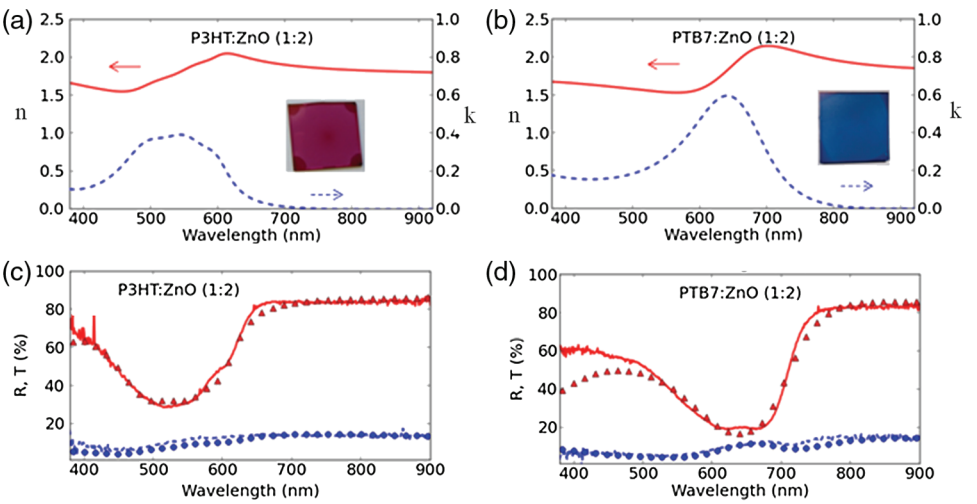

Figure 8 Optical indices n (continuous lines) and k (dotted lines) as a function of the wavelength λ for (a) P3HT:ZnO (1:2) and (b) PTB7:ZnO (1:2) layers coated on glass substrates. (Insets are photographs of the samples.) (c) and (d) Comparisons between experimental measurements of T (-) and R (. . .) and optical simulations of T (Δ) and R (O) for layers coated on glass substrates: (c) P3HT:ZnO (1:2) and (d) PTB7:ZnO (1:2) (extracted from Ref. 42).

simulations, the optical indices obtained by SE [cf. Figs. 8(a) and 8(b)] and the film thicknesses measured using a mechanical profilometer were used as input parameters. The P3HT:ZnO (1:2) layer was 120-nm thick and the PTB7:ZnO (1:2) layer was 150-nm thick. These thickness values are coherent with those currently used in OSC devices. A good agreement between the calculated and the measured spectra demonstrates the reliability of these optical indices n and k to predict the real optical properties of the films.

A very recent study has shown that a sum of Gaussian oscillators can be used to model the imaginary part of the dielectric function of organic semiconductors such as PC60BM ([6,6]-phenyl-C61-butyric acid methyl ester) and PC70BM ([6,6]-phenyl-C71-butyric acid methyl ester).[42] Figure 9(a) shows the imaginary part of the dielectric constant of PC70BM and the Gaussian oscillators that were used for the dispersion model elaboration. Because Gaussian oscillators are suitable to describe strong electron–phonon coupling in π-conjugated molecules, they are used to model the absorption line shape for organic semiconductors. Thus, a Gaussian-based dispersion model made it possible to extract the electronic transitions for PC60BM and PC70BM in the UV–visible range.[42] The table in Fig. 9 gives a comparison between the transition energies extracted from the position of the Gaussian oscillators within the dispersion model of PC70BM[42] and those extracted from spectrophotometric measurements.[43–45] A very good agreement between electronic transition values obtained from SE measurements and literature data demonstrates the reliability of the dispersion model and shows the potential of SE measurements for the determination of the optoelectronic properties of materials. Thus, these results show that SE is of high interest not only for nondestructive measurements of thicknesses and optical indices but also for nondestructive measurements of the electronic transitions in materials within thin-film stacks.

(a)

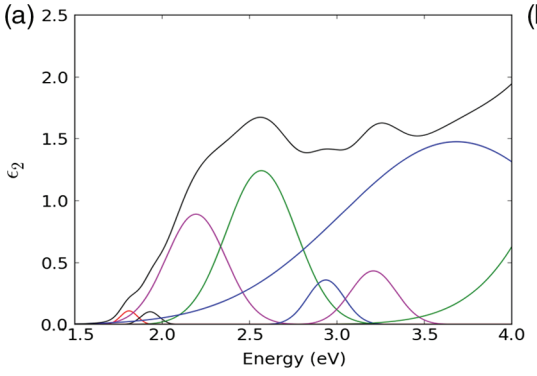

(b)

Peaks	Energy (eV)	Energy (eV) Ref.
Gaussian 1	1.807 ± 0.001	1.80 [12]
Gaussian 2	1.9253 ± 0.0009	1.90 [10]
Gaussian 3	2.1926 ± 0.0004	2.2 [10]
Gaussian 4	2.566 ± 0.001	2.55 [10]
Gaussian 5	2.934 ± 0.003	-
Gaussian 6	3.206 ± 0.004	3.2 [10]
Gaussian 7	3.687 ± 0.001	3.75 [11]
Gaussian 8	5.222 ± 0.002	-

Figure 9 (a) Imaginary part of PC70BM and Gaussian oscillators that have been used for the dispersion model elaboration (extracted from Ref. 42) and (b) Gaussian oscillator positions extracted from the dispersion model of PC70BM (extracted from Ref. 42).

3.3 Photoluminescence

Luminescence-based techniques are the family of techniques that investigate the emission of light from a solid due to the deviation of the system from the thermal equilibrium. In particular, PL relates to the deviation of the equilibrium via the absorption of light with an energy higher than the bandgap of the material.

The PL spectrum is caused by the relaxation of electrons—previously excited to the conduction band by the incident light—to lower energy states and the simultaneous emission of photons. Not all the possible relaxation processes will generate photons, since the transition should be dipole-allowed for a successful photon emission to occur. Among them, there is a set of different transitions that are possible to see in a semiconductor used in photovoltaics (these transitions are summarized in Fig. 10). To determine the transition rate of these relaxations, calculations applying the first-order perturbation theory are needed, as explained in more detail in Ref. 46. In general, the emission yield of any transition is as follows:[47]

$$Y_{\mathrm{PL}}(L) = L^k, \tag{9}$$

where L is the power of the light excitation and k is a parameter that depends on the nature of the transition. The values that k can adopt are generally between 0.5 and 2. The position of the maximum of the peak may also be modified with the excitation intensity, giving more information about the nature of the transition.

The study of the evolution of the peak luminescence with the temperature also informs about the nature of the transition. The peak yield normally decreases with the increase in temperature, a phenomenon known as PL quenching, and, as a result of the evolution of the bandgap with the temperature, there will be a redshift of the transition energy position with the increase in temperature.

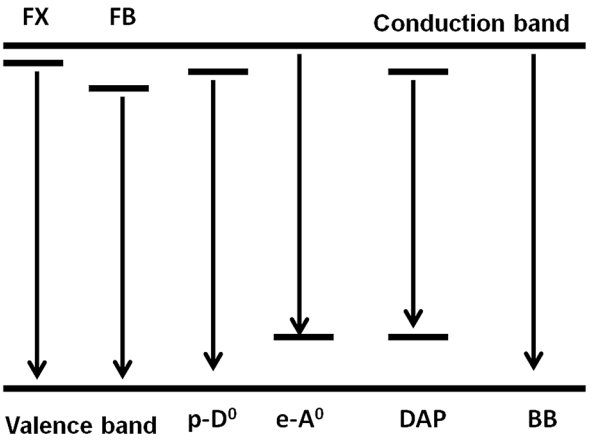

Figure 10 Schematic representation of the different origins of transitions that can be observed by PL. From left to right the free (FX) and bound (FB) excitonic transitions, the free-bound transitions (p-D^0 and e-A^0), the DAP and the BB transitions.

The PL quenching can be described with the following equation:

$$Y_{\mathrm{PL}}(T) = \frac{1}{1 + Ce^{-E_a/kT}}, \tag{10}$$

where E_a is the activation energy of the transition and C is a constant that, in the case of a transition where either the valence or the conduction band is involved, is proportional to $T^{3/2}$.[48]

We can separate the transitions shown in Fig. 10 in three different groups, depending on the nature of the levels involved: the excitonic transitions (FX and FB), the free-bound transitions, the donor–acceptor pairs (DAP) and the band–band (BB) transitions.

3.3.1 Excitonic transitions

When the PL measurement is performed at a low enough temperature, transitions with a very low excitation energy, which cannot be observed at RT, such as the recombination of an electron–hole pair bounded by the Coulomb interaction, become measurable. These transitions are called free exciton transitions. The exciton binding energy can be calculated from a hydrogenic model, as shown in Ref. 46. The energies obtained for classical semiconductors are on the order of 10 to 15 meV. These energies being smaller than kT, the quenching of the exciton luminescence happens at low temperatures. But, for organic semiconductors, the binding energy of the exciton is comparable to the thermal energy at RT, and excitons are observed at RT.[49] In the case of perovskites, there is much discussion about the nature of the transitions observed at RT in PL. While there are calculations that predict energies around 50 meV, that should allow their observation at RT,[50] experiments are less conclusive, giving results in both directions.[26,51,52–54]

When the evolution of the PL yield with the excitation power is analyzed, it should be expected that the excitonic transitions present a k value of 1 in the resonant state, but Schmidt et al.[47] showed that k can adopt any value from 1 to 2, depending on the material. Excitonic transitions do not exhibit any shift in position with increasing excitation intensity.

Free excitons can be bound to either acceptor or donor impurities, and they become bound excitons. The ratio between bound and free excitons depends on the material, the temperature of measurement, and the sample doping level.[46]

Bound and free excitons behave alike when they are studied at different excitation powers.[47]

3.3.2 Free-bound transitions

In real semiconductor materials, one can expect to find localized states related to acceptor or donor impurities, which may create transitions with the free carriers in the bands. These transitions occur either between the conduction band and an acceptor level (e-A^0) or between the valence band and a donor level (p-D^0).

When studying the transition dependencies on the excitation power, k should be equal to 1, as the recombination should be proportional to the free carrier generation rate in the bands, which depends linearly on the excitation power.

For thermal quenching, free-bound transitions are still described by Eq. (10), but now the energy E_a represents the ionization energy of the impurity. Thus, the peak position is modified when the temperature changes.

3.3.3 Donor–acceptor pairs

In semiconductors with a high enough defect density, it is possible to observe transitions between two defect states.

DAP transitions show a different behavior with excitation intensity from the previously studied transitions. The peak position of a DAP depends on the level of injection, as follows:[55]

$$E_{\mathrm{DAP}}(L_{\mathrm{exc}}) \propto E_{\mathrm{DAP}}(L_0) + \beta \log\left(\frac{L_{\mathrm{exc}}}{L_0}\right), \tag{11}$$

where β is a proportionality factor, with values typically between 1 and 5 meV. This means that the peak will experience a blueshift when the excitation intensity increases. For the parameter k, the values are smaller than 1.[47]

The thermal quenching of the DAP intensity is also different from the other transitions:

$$Y_{\mathrm{PL}}(T) = \frac{1}{1 + C_1 e^{(-E_{a1}/kT)} + C_2 e^{(-E_{a2}/kT)}}. \tag{12}$$

Here, we have two exponential terms, each corresponding to one impurity. When the constants C_1 and C_2 are similar, the first activation energy corresponds to the shallower impurity.[48]

3.3.4 Band–band transitions

When the temperature is high enough, both excitons and impurities are ionized and the valence and conduction bands become more populated with photoexcited electrons. In this situation, the probability of observing BB transitions increases. As these transitions are between the conduction and valence bands, and because both populations are dependent on the excitation intensity, the value of parameter k can be larger than 1. In the limit of high injection, where BB transitions are the dominating recombination, k is equal to 1.

All these transitions can be found in most semiconductors, but in the case of semiconductors composed of many atoms, such as CIGSe or CZTSe, the high concentration of donor and acceptor impurities leads to the overlapping of the wave functions of these impurities, creating impurity-related bands. When donor and acceptor densities are similar, the semiconductor is compensated, with a net carrier density much smaller than the impurity densities. As the distribution of the defects

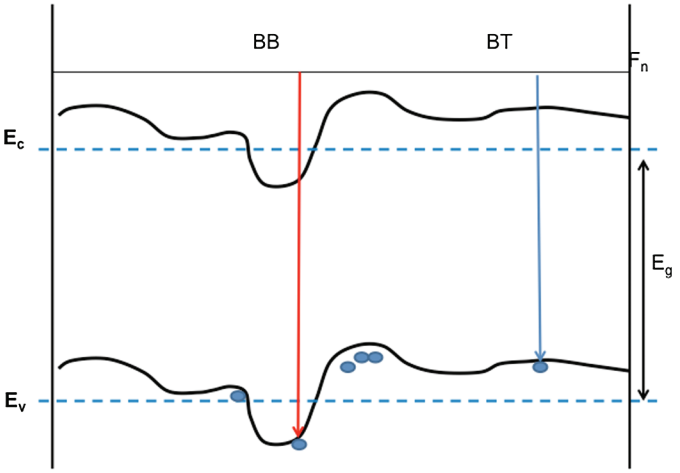

Figure 11 Diagram of the model of potential fluctuations on the bands of a semiconductor showing the BB (red) and band-trap transitions (BT, blue) as explained in Ref. 56. This model is generally applied to explain luminescence properties of multinary semiconductors such as CIGSe and CZTS.

in the lattice is not homogeneous, the bands start to get deformed because of the strong local variations of the electrical field that cannot be screened by the net carrier density. This potential fluctuation affects the optoelectronic properties of the material, allowing certain transitions with a much smaller energy than DAPs or free-bound transitions. The impact of this potential fluctuation is shown in Fig. 11.

When studying transition dependencies on the excitation power variations, potential fluctuation transitions show a k parameter smaller than 1, but larger than the one expected for a DAP. Also, the strong blueshift with the excitation power is very specific of these transitions—it is normally one order of magnitude bigger than the one corresponding to a DAP.

When the temperature is increased, the evolution of the peak gets more complex than for the other cases. At the beginning, the peak undergoes a redshift, but if the experiment continues toward higher temperatures, then a blueshift occurs. One possible explanation is that for very low temperatures, the charges are frozen in the different wells without the possibility of moving, so the lowest energy levels are not completely filled. As the temperature increases, the higher thermal mobility of the charges is such that the lowest levels are filled, leading to photon emission with lower energies than before. Finally, when the temperature keeps increasing, more distant charges are thermally emitted up to the band, leaving the closer pairs, thus producing higher energy recombination centers.[56]

As an example of the PL of a potential fluctuation material, in Fig. 12, we can observe PL evolution as a function of the excitation power (a) and temperature (b) for a Cu_2ZnSnS_4 (CZTS) solar cell. Both the strong blueshift and the k value

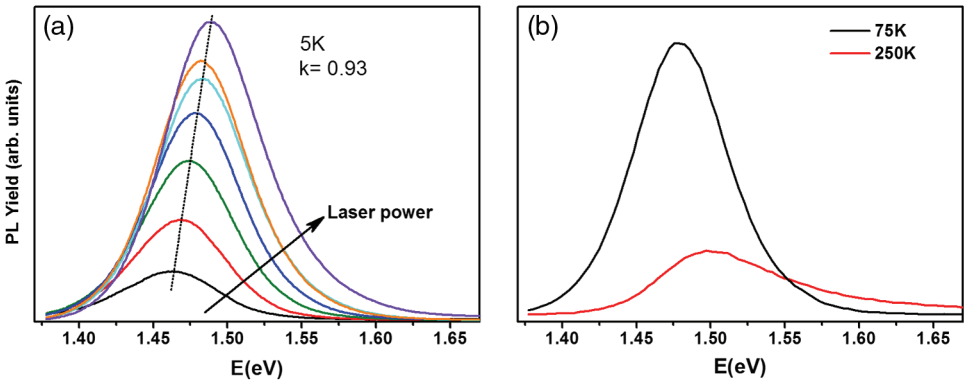

Figure 12 PL evolution with the (a) excitation power and (b) for two different temperatures for a Cu_2ZnSnS_4 solar cell. The blueshift in both cases is very strong showing the behavior of the potential fluctuation model.

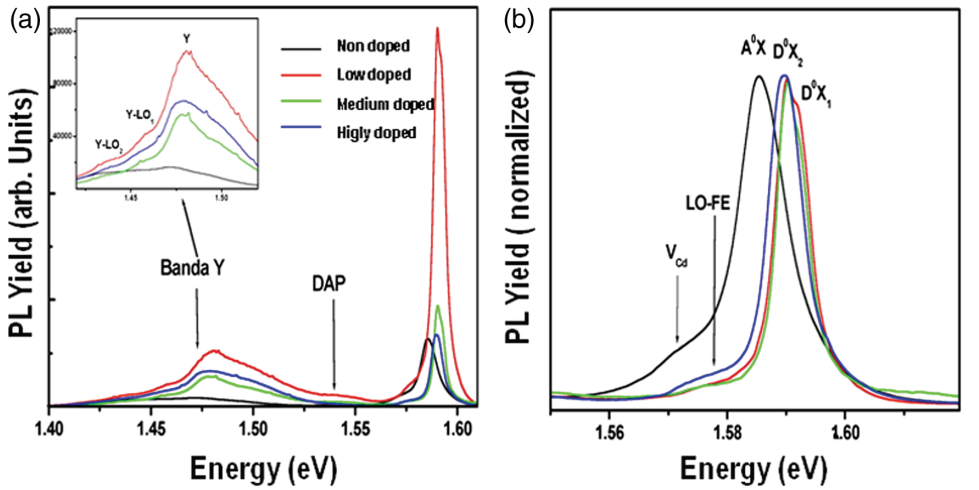

Figure 13 PL spectra for CdTe thin films doped with different quantities of (a) bismuth measured at 12 K. The excitonic region appears between 1.59 and 1.6 eV, and a DAP at 1.53 eV. At lower energies the Y band appears: it is related to the structural dislocation associated with the inclusion of such a big atom in the lattice. (b) A detail of the excitonic region, where the change in defect binding, from an acceptor bound for the nondoped sample to a donor bound for the Bi-doped sample, is shown.[57]

obtained when the excitation power is increased are in agreement with the potential fluctuation model. It is also worth comparing the shapes of the peaks for the CdTe shown in Fig. 13 and the CZTS layers in Fig. 11: for CdTe, we observe very well defined peaks corresponding to the particular transitions. For the potential fluctuation materials such as CZTS, peaks are much broader, with energies that are more difficult to determine.

3.4 Photoreflectance

While PL is a technique that studies the interaction between the semiconductor and light, and needs a minimal amount of material to provide an interpretable signal, reflectance-based techniques exploit the sudden variation of the optical indices at an interface. This means that they are much more sensitive to small quantities of material and can obtain information on what is really happening at the interface between two different materials.

PR belongs to the family of modulated reflectance techniques such as ER or piezoreflectance. The main advantage of PR is that, as it uses an optical modulation, the whole setup is optics based, and does not require any previous preparation of the sample for analysis such as contact deposition.[58,59]

Modulated reflectance techniques consist of the measure of the reflectance at an interface, while the effective electrical field applied on this interface is modulated externally. When PR is used, the electrical field is modified by the modulated injection of photons with an energy higher than the bandgap,[60] which in experimental setups is provided by a laser pump. When the semiconductor absorbs a photon, an electron is promoted to the conduction band and the redistribution of charges near the interface is equivalent to a modulation of the electrical field. While the interface is modulated by the pump, the sample is scanned at different wavelengths with a secondary light source and the resultant reflectance is recorded. The PR signal is defined as the ratio between the reflectance measured when the pump is illuminating the sample and the reflectance when the pump is off. The final PR spectrum is composed of sharp three-derivative-like features that appear at the energy position corresponding to the interband optical transitions of the material.

It is worth noting that, while PL measures the optical transitions within the bandgap of the semiconductor, PR is able to identify further interband transitions, these two techniques being complementary for the whole optical characterization of a system. It is also interesting that both techniques can be performed in the same setup, as the modulated pump of the PR can be the source for a PL experiment, so that both spectra are measured under the same conditions.[61]

Like all the modulated reflectance techniques, PR allows the measurement of the fundamental bandgap transition with precision, and because there is no shifting of the features related to the experiment conditions, it is more reliable than PL.

Because the interaction of the light with the material occurs at the interface, this technique is very sensitive to any phenomenon happening there, such as interdiffusion of species, formation of mixed alloys, and presence of secondary phases. It can be a very powerful tool for characterization of thin-film-based solar cells, where normally the p-n junction is formed by two different semiconductors. On the other hand, as was previously stated for the ellipsometry, reflectance-based measurements are very sensitive to the roughness of the surface, which limits

the effectiveness of the technique for very rough surfaces. In the case of PR, this leads to a less intense signal and broader peaks.[62]

3.4.1 Photoreflectance on a $CuInS_2$ solar cell system

To analyze the origin of J_{sc} deviations in a set of $CuInS_2$/CdS solar cells fabricated in the same nominal conditions, PR measurements were performed in the devices and compared with structural and electrical characterizations.[63] When PR spectra were obtained for a low and a high J_{sc} device, the resulting transitions were different, as can be observed in Fig. 14. For the lower J_{sc} cell, both transitions appear clearly, one, E_a, corresponding to the fundamental bandgap of the CIS, and a second one, E_b, corresponding to the transition between the conduction band minimum and the Γ_5 band in the valence band.[64] In the high J_{sc} solar cell, both transitions overlap. In fact, as is explained in Ref. 64, for the CIS, both valence bands Γ_4 and Γ_5 are involved when the material is fully relaxed, but in our case, band splitting up to 60 meV occurs for the lower J_{sc} devices. This result shows that there is a relationship between the strain the layer is subjected to and J_{sc}

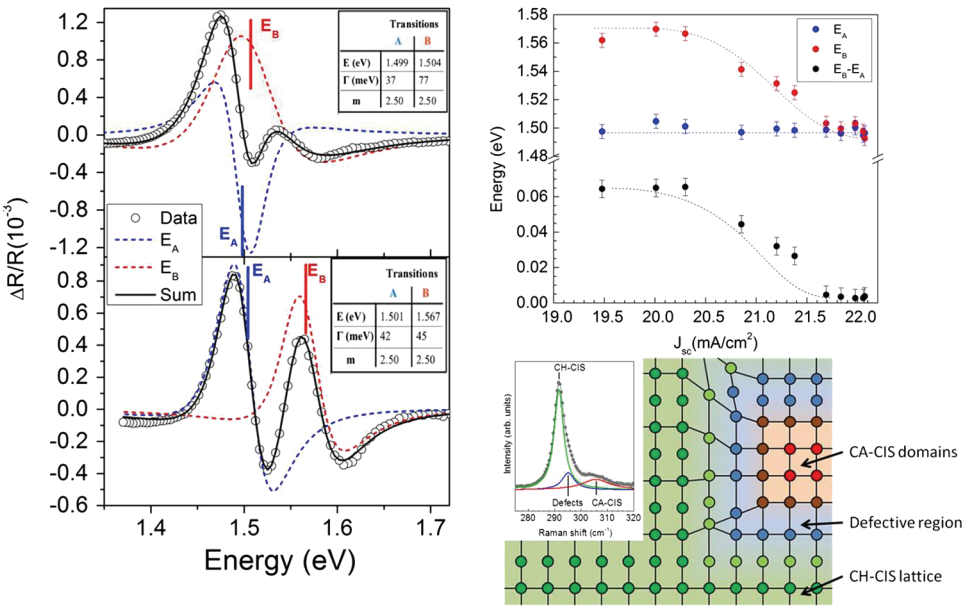

Figure 14 On the left, PR spectra for a high J_{sc} CIS solar cell (top) and low J_{sc} CIS solar cell (bottom) with the corresponding fittings for EA and EB. At the top right, the representation of both EA (the bandgap) and EB as a function of J_{sc} and their corresponding energy splitting in the valence band (EB–EA). At bottom right, the Raman scattering spectrum for the high J_{sc} that shows the presence of the Cu–Au CIS phase in coexistence with a defective region. This CA-CIS and the defective region concentrate most of the structural defects, leaving the CH-CIS less defective and improving its transport properties. Images are extracted from Ref. 63.

losses. By studying the Raman scattering of these layers, we observed that the samples with better J_{sc} exhibited small fractions of CIS Cu–Au phase (CA), leading to the conclusion that the presence of certain amounts of this defective phase helps to minimize the strain in the chalcopyrite (CH) phase of CIS, improving its transport properties.

3.4.2 Combination of photoreflectance and photoluminescence for studying the bandgap of perovskite layers

As has been stated before, PR gives a very accurate measure of the fundamental optical bandgap of the semiconductor. It is particularly useful when complementary information, like PL peak positions, can turn out to be contradictory. In this example, a set of organometallic perovskites, $CH_3NH_3PbCl_x(I_yBr_{1-y})_{3-x}$ with different I/Br ratio is studied both by PL and PR.[51]

In Fig. 15, both the PL power dependence analysis at RT and the PR spectrum from the pure I sample, $CH_3NH_3PbCl_xI_{3-x}$, are presented. From the PL on the left in Fig. 15, we can see that the evolution of the peak intensity with the laser power gives a k of 1.33 (inset). Also there is no shift of the peak position. Both behaviors are consistent with an excitonic-like transition, as explained in Section 3.3. On the PL spectrum, it is possible to observe the presence of excitons in the perovskite layers, as the calculated exciton binding energy is about 50 meV,[49] an energy large enough to permit its measurement at RT. The PL peak maximum appears at 1.61 eV, not far from the bandgap value that we extract from the PR spectrum presented in the right in Fig. 15.

Similar results are obtained for the pure Br layer, $CH_3NH_3PbCl_xBr_{3-x}$, with values of 2.35 eV for the maximum PL peak position and 2.27 eV for the bandgap extraction from the PR spectrum. The k factor, 1.4, is also of the same order.

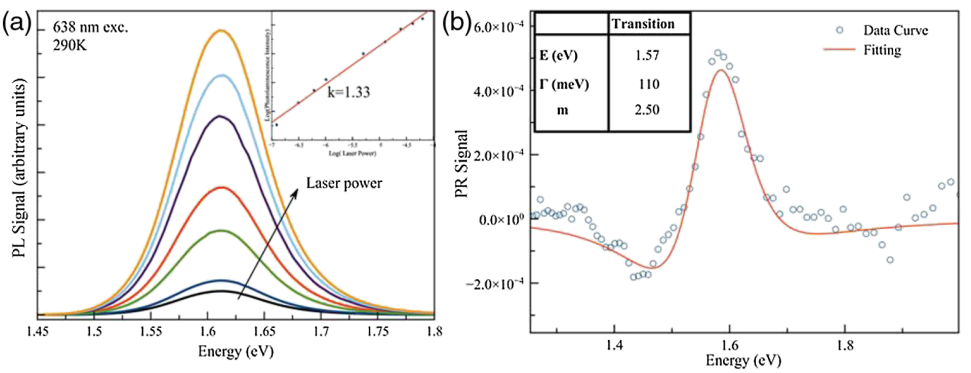

Figure 15 (a) PL power dependence analysis for the pure iodine perovskite, $CH_3NH_3PbCl_xI_{3-x}$. The peak maximum position does not shift, and the plot of the PL yield versus the laser intensity gives a slope of 1.33, indicating that the transition is excitonic-like. (b) The PR spectrum for the same sample, giving a value of 1.57 eV for the bandgap.[51]

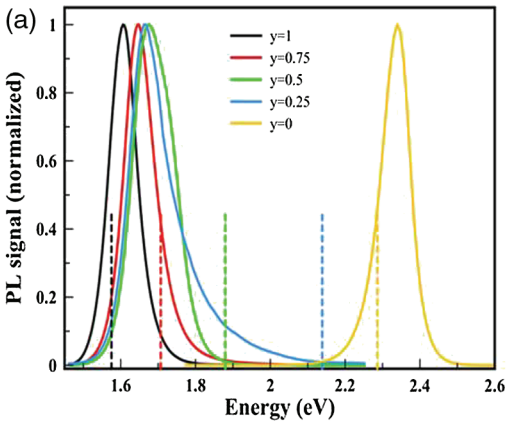

(b)

Y	Peak maximum (eV)	K(PL)	Band Gap PR (eV)
0	2.35	1.4	2.27(3)
0.25	1.72	1.58	2.19(3)
0.5	1.74	1.66	1.88(5)
0.75	1.68	1.55	1.64(5)
1	1.61	1.33	1.57(2)

Figure 16 (a) PL peaks for different I/Br ratios in $CH_3NH_3PbCl_x(I\ Br_{1-y})_{3-x}$. Dotted lines of the same color as the PL peak indicates the bandgap position calculated from PR spectra. (b) A recapitulation table with the PL peak positions, the PR bandgaps, and the *k* values from the PL power dependence study for all the compositions.[51]

Nevertheless, the situation changes for the mixed alloys. In Fig. 16, a graph with the different samples PL peak and the bandgap position calculated from the PR spectra for each sample are plotted. While the two pure samples present the same behavior (the PL peak overlapping the PR bandgap position), for the mixed alloys, the PR bandgap position follow the expected distribution, while the PL peaks are all red shifted and very near to the pure iodine peak. In the table on the right in Fig. 16, we can see the discrepancies between the PL maximum position and the PR bandgap, as well as the *k* parameter for the PL power dependence study for all the samples. The reason for the shifting of the PL spectra is not yet clear. While *k* suggests an excitonic-like transition, the difference in energies between the peak maxima and the bandgap values could be accounted for by the presence of bound excitons relative to a deep-level defect, which is not very likely. On the other hand, there are studies showing the decomposition of the mixed alloys occurring in the cell with pure compositions.[65] In that case, we would use PR to measure the bandgap at the surface where composition is not very affected, while PL is generated by a much larger volume of material, where the decomposition takes place.

4 Simulation Tools for Predicting Solar Cell Performances

4.1 Optical modeling

To reach the objective of controlling the light inside the cell, numerical and analytical methods can be used to predict and optimize the optical properties of solar cells under standard lighting conditions. First, optical simulation tools allow us to maximize the photonic absorption inside the thin active layers of the cells. Color

properties provided by new organic materials combined with their intrinsic mechanical properties would allow the emergence of a new industry involved in the integration of electronic components. Thus, a better control of the OSC colors could also play an important role for new applications such as power generating bags, laptops, mobile phones, and for fashion and architectural applications.

A reliable optical model would require at least three input parameters: the optical index spectra of the materials [$n(\lambda)$ and $k(\lambda)$], the emission spectrum of the light source, and a mathematical interpretation of the human eye sensitivity. The optical indices of the materials are generally obtained by SE measurements. For outdoor applications, the global tilt AM1.5 spectrum from[66] is generally used as the reference for PV engineering. It represents the solar spectrum received at sea level and at a zenith angle of 48.19 deg by a surface tilted 37 deg and facing the sun. For indoor applications, it would be necessary to measure the emission spectrum of the lighting sources studied. The assignation of colors proceeds from the sensitivity of the human visual system and then from the interpretation by the human brain. This psychophysical process can be described by several models, such as the xyY CIE 1931 model.

Although optical performance investigations require the calculation of the total number of photons absorbed in the active layer of the cells, the color and transparency perception results from the perception of the luminous energies reflected and transmitted by the cells. The TMM is an analytical method that allows the optical modeling of thin films in one dimension (1D). Thanks to a matricial formalism, one can access the total reflection $R(\lambda)$ and transmission $T(\lambda)$ spectra of thin-film stacks and the number of photons absorbed in each layer of the stacks.[67] It is a fast method which has proved its reliability to model the optical properties of thin-film solar cells such as organic and hybrid organic/inorganic solar cells.[41,42,68,69] 2D and 3D modeling can be realized using several methods such as finite element (FE), FDTD,[5] or rigorous coupled wave analysis (RCWA).[70] These methods are used for nonplanar thin films and are widely implemented to study photonic structures such as plasmonic structures[70–72] or photonic crystals[69,73,74–76] able to confine the light in the active layer of ultrathin solar cells.

4.1.1 Photonic crystals to trap the light in the active layer of organic solar cells

Figure 17(a) shows an OSC architecture integrating a double structured photonic crystal slab (PC OSC). The active layer is composed of a TDPTD:PCBM blend, where TDPTD refers to poly(3-(2-methyl-2-hexylcarboxylate)thiophene-co-thiophene). In this design, the PEDOT:PSS interface layer (poly(3,4-ethylenedioxythiophene) poly(styrenesulfonate)) and the silver (Ag) back electrode are both structured in the shape of subwavelength gratings. Figure 17(b) shows a comparison between the photonic absorption spectra of an optimized planar OSC and an optimized PC OSC calculated through FDTD modeling.[5] In both cases, the photonic absorption has been specifically calculated inside the active layer. This figure shows that an

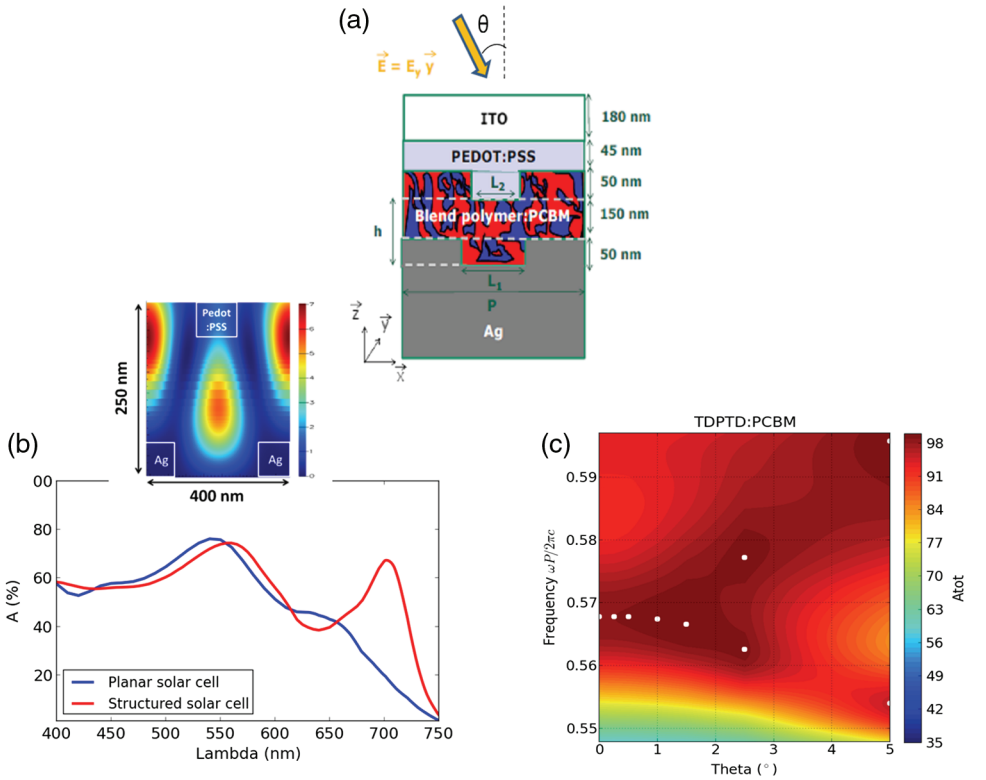

Figure 17 (a) A schematic view of an OSC architecture integrating a double structured PC slab: both the PEDOT:PSS layer and the silver are structured; (b) a comparison between the photonic absorption in planar OSCs and in 1-D PC OSCs based on TDPTD:PCBM. The inset is a cartography of the electric field intensity inside the 1-D PC slabs at the resonance wavelength (λ = 704 nm); (c) a color map giving the total absorption spectra of the 1-D PCs solar cell as a function of both the incident angle θ and the reduced frequency (ω*2πc/*P*). (Source: All these figures have been extracted from Ref. 5.)

absorption resulting from a Bloch mode coupling (peak at λ = 704 nm) clearly boosts the absorption of the PC OSC. The inset of Fig. 17(b) shows a cartography of the electric field intensity ($|E(\lambda, x, y, z)|^2$) inside the active layer. White squares have been added in this cartography to show the position of the gratings in Ag and in PEDOT:PSS inside the active layer. The photonic absorption $A(\lambda, x, y, z)$ at each position (x, y, z) within the PC OSC is directly proportional to $|E(\lambda, x, y, z)|^2$:

$$A(\lambda, x, y, z) = \frac{n(\lambda, x, y, z)}{n_0} * |E_{\text{norm}}(\lambda, x, y, z)|^2, \tag{13}$$

where n_0 and $n(\lambda, x, y, z)$ are the refractive indices of the incident medium and at position (x, y, z), respectively, and $E_{\text{norm}}(\lambda, x, y, z)$ is the normalized electric field. Thus, the electric field intensity cartography shown in Fig. 17(b) proves that the

Bloch mode coupling has been optimized to increase the photonic absorption inside the active layer while minimizing the losses inside the Ag and the PEDOT:PSS gratings. Figure 17(c) shows a color map displaying the total absorption spectra of the PC OSC as a function of both the incident angle θ and the reduced frequency. The white points give the absorption peak positions. A unique absorption peak appears at the low values of θ and two absorption peaks appear for θ values higher than 1.5 deg. These results show that it is possible to obtain multiple Bloch resonances in the case of a large incidence cone. Finally, by integrating the absorption spectra averaged on an 8-deg incident cone, the authors obtained an absorption gain around 15% using a PC OSC.[5]

4.1.2 Color-tuned, highly efficient, organic solar cells

The results presented in Fig. 18 concern color and performance investigations of PTB7:PC70BM-based OSCs in a standard architecture [cf. Fig. 18(a)] through optical simulations using a TMM.[69] The aim was to control the interferential phenomena occurring in such a thin-film solar cell by varying the thicknesses of the active layer and of the ZnO electron transporting layer in the 0 to 300 and the 0 to 90 ranges, respectively. The thicknesses of the other layers were kept constant: 150 nm for the ITO transparent anode, 45 nm for the PEDOT:PSS hole-transporting layer, and 200 nm for the Al back electrode. The optical indices of all the layers were measured by SE.[68,69,75]

The diagram in Fig. 18(b) gives the total number of photons absorbed inside the active layer under an AM1.5 illumination as functions of the ZnO layer thickness and of the active layer thickness. The different curves correspond to different values of ZnO thickness. For each value of ZnO thickness, two maxima and two minima appear in the absorption curves. These modulations are due to interferential phenomena occurring in thin-film stacks.[5,68,69] Figure 18(c) shows the different colors that can be produced by varying the thicknesses of these two layers. It is a color representation based on the CIE xyY (1931) model.[69] The three curves of the diagram correspond to three ZnO thicknesses (0, 20, and 80 nm). Each curve depicts the color evolution of the devices according to the active layer thickness. For easy reading, a white arrow indicating the increase in the active layer thickness was added on the chromaticity diagram. These results show the possibility to control the color of devices by adjusting the thicknesses of both the ZnO and the active layers. For the thin ZnO layers (0 and 20 nm), the devices are successively green, light blue, yellow, and orange when the active layer thickness is increased. For an 80-nm thick ZnO layer, the devices become successively blue, yellow, and navy blue when the active layer thickness is increased. By combining the results from the optical performance investigations [Fig. 18(b)] and those from the color predictions [Fig. 18(c)], the authors selected three cases of solar cells. Figure 18(b) gives the thickness values for the ZnO and the active layers for these three solar cells G, Y, and B. The G, Y, and B solar cells were experimentally realized and exhibited PCEs of 6.73%, 7.10%, and

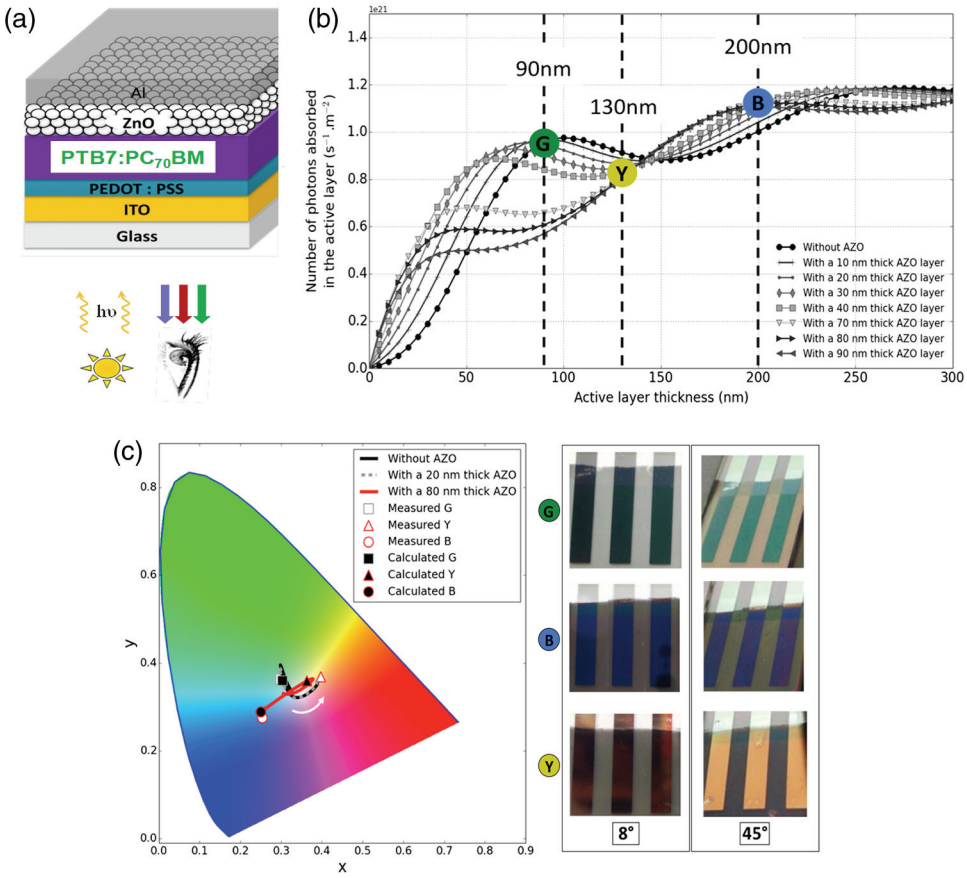

Figure 18 (a) Schematic representation of a PTB7:PC70BM-based OSC in a standard architecture, (b) theoretical absorption in the active layer as a function of the active layer thickness (B, Y, and G refer to the solar cells studied) (extracted from Ref. 69), and (c) predicted color as a (left) function of active layer and ZnO thicknesses and (right) photograph images of the green, blue, and yellow solar cells at 8 deg and 45 deg (source: extracted from Ref. 69).

7.59%, respectively. A comparison between the calculated and the measured color coordinates of the three solar cells at an angle of 8 deg is shown on the chromaticity diagram in Fig. 18(c). The inset of Fig. 18(c) shows photograph images of the three solar cells G, Y, and B under different observation angles.

4.2 Optoelectronic simulation

As previously stated, the possibility of modeling the interaction of light with each layer in a solar cell means that it will be possible to optimize traditional devices and design new ones based on thin-film materials. Nevertheless, the whole performance of a solar cell involves the coupling of the light absorption and the electrical properties of the materials. Furthermore, optoelectrical properties such as the

bandgap have major implications in the electrical performance that cannot be foreseen with only optical modeling. In this section, we will show how it is possible to predict the performance of the devices with simple models, taking into account the electro-optical coupling.

The main equations describing a semiconductor system are the Poisson equation

$$\nabla \cdot (\varepsilon \nabla \Psi_{\text{vac}}) = -\rho, \tag{14}$$

where Ψ_{vac} is the potential of the system related to the vacuum level energy and ρ is the charge density, and the continuity equations for electrons and holes

$$\frac{\partial n}{\partial t} = \frac{1}{q} \nabla \cdot \vec{J}_n + G - R, \tag{15}$$

$$\frac{\partial p}{\partial t} = -\frac{1}{q} \nabla \cdot \vec{J}_p + G - R, \tag{16}$$

where n and p are the electron (n) and hole (p) concentrations, J_n and J_p are the corresponding current densities, t is the time, R is the recombination rate that can be modeled as a function of the defects in the bulk of the materials, and G is the generation rate, created by the incident light and thus calculated following the methods presented in Section 4.1.

We can describe the electron and hole current densities as a function of the respective concentrations and the quasi-Fermi levels

$$\vec{J}_n = \mu_n n \nabla E_{Fn}, \tag{17}$$

$$\vec{J}_p = \mu_p p \nabla E_{Fp}. \tag{18}$$

By using the Maxwell–Boltzmann distribution, we can write both n and p as a function of these quasi-Fermi levels and the respective effective density of states in the valence band (N_{V}) and conduction band (N_{C})

$$n = N_{\text{C}} e^{\left(\frac{E_{Fn} - E_{\text{C}}}{kT}\right)}, \tag{19}$$

$$p = N_{\text{V}} e^{\left(\frac{E_{Fv} - E_{\text{V}}}{kT}\right)}. \tag{20}$$

In equilibrium, the product of the charge densities has to be equal to the intrinsic carrier concentration of the semiconductor. When solving the equations, boundary conditions have to be imposed; in our case these boundaries are the contacts, which can be ohmic (flat band condition) in an ideal case, or present some degree of rectification implemented as an energy barrier.

For correctly solving these systems, we are in need of many more parameters than in the pure optical modeling, varying from more general ones, such as the

bandgap or the electron affinity, to some more specifically related to the electrical properties that can also be very dependent on the process of fabrication of the device, such as charge mobilities or intrinsic carrier concentrations.[77,78] This means that the results will be very parameter dependent, which has to be taken into account when they are interpreted. To show that the results are reliable, it is recommended to compare—and validate—them with experimental results when it is possible.

These calculations can be carried out in one-dimensional models, or multidimensional systems, allowing a better approximation of the reality at the expense of computer power and time. There are many commercial and public codes that can be used for this type of modeling.

4.2.1 Impact of the band alignment in a heterostructure: the CIG(SSe) system

The CIGSe solar cell is a heterostructure, as has been shown previously (see Section 2.2). In the p-n junction, two different semiconductors are in contact, generating a misalignment of the conduction band that has been widely known as a source of limitation for device performances.[34,79,80,81] The differences in bandgap and electron affinity between the absorber and the buffer layer lead to an abrupt change in the continuity of the conduction band, which can be positive (spike) or negative (cliff), as can be seen in Fig. 19 for the case of pure $CuInSe_2$ and $CuGaSe_2$ with a CdS buffer layer. These secondary barriers contribute to the accumulation and recombination of charges in the CdS/CIGS interface, leading to a decrease in the J_{sc}, combined with a reduced FF, because of the impact of these recombinations in the final series resistance. The formation of important secondary barriers in the junction with the CIGS is the main reason CdS is still the

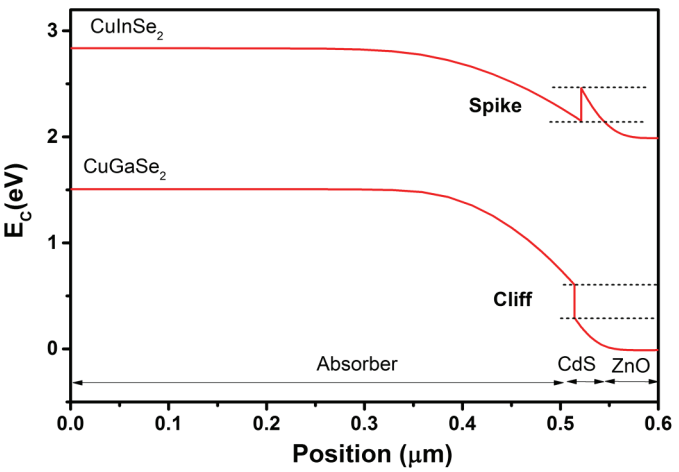

Figure 19 Effect of the difference bandgap and electron affinity on the interface band alignment of the conduction band for CISe (top; bandgap 1.01 eV, χ 4.5 eV) and CGSe (bottom; bandgap 1.68 eV, χ 3.89 eV) with CdS (bandgap 2.45 eV, χ 4.2 eV). The calculations have been performed with SCAPS1D.[82]

preferred buffer layer despite the presence of cadmium and the relatively low bandgap compared with other candidates such as ZnS or In_2S_3.[79]

For the standard CIGSe/CdS solar cell, where the bandgap near the interface is about 1.1 eV,[80,83] the value of the spike is about 0.2 eV, which still has some impact on the final performance. One strategy that has been used in the industry for decreasing this value is to add sulfur to the surface of the CIGSe layer.[84,85] The inclusion of sulfur increases both the material bandgap and electron affinity, leading to a smaller energy difference between the absorber and CdS conduction bands[85] and reducing the spike barrier created at the junction.

The impact of the band alignment on the performance of the cell can be calculated in a 1D model. In Fig. 20, the band structure at the absorber/buffer interface is

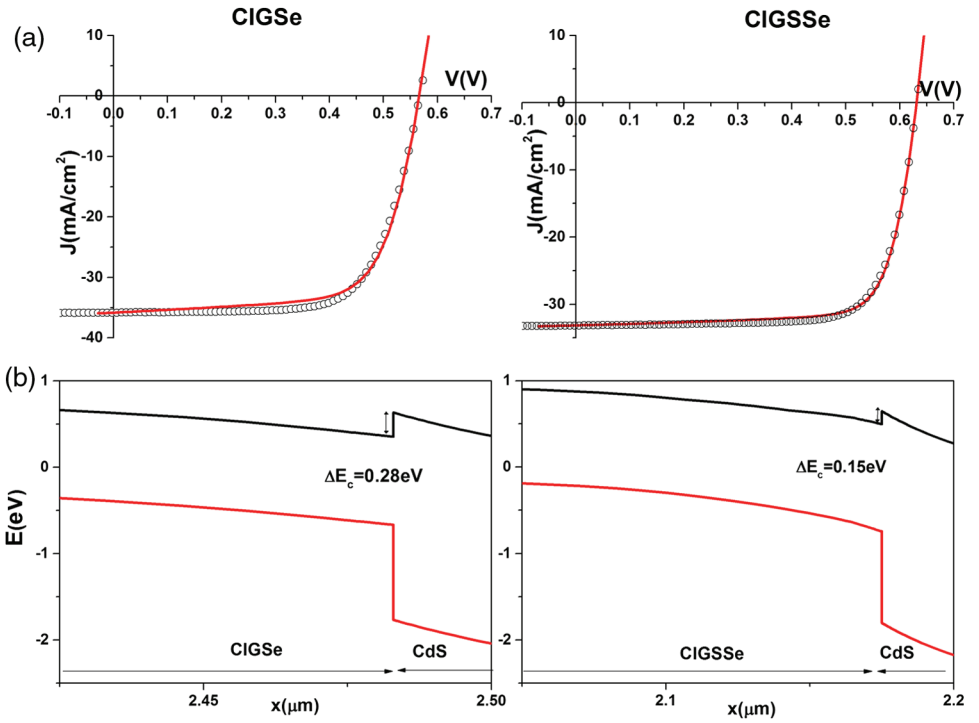

Sample	J_{sc} (mA/cm^2)	V_{oc} (mV)	FF (%)	η (%)
CIGSSe	33.2	631	75.54	15.8
CIGSe	35.8	568	69.47	14.1

Figure 20 Band alignment in the absorber/buffer interface region for (a) a pure CIGSe absorber and (b) a sulfur-rich CIGSSe with the corresponding experimental and modeled *JV* curves. The value of the spike is reduced by half by the sulfur inclusion. The improvement in the band alignment leads to a better FF and an efficiency increase of more than 1.5 points. Table with the photovoltaic parameters of both cells at the bottom. These results have been obtained with SCAPS1D[86] and published.[81]

presented for two different solar cells, one with no sulfur in the CIGSe and another one with an S/(S + Se) ratio of 0.48. The main difference is the reduced value of the spike for the sulfur-rich cell, which is almost half that for the pure selenium cell. As can be observed in the inset, the modeled *JV* curves are in agreement with the experimental ones. Because the CdS layer is the same for both cells, the increase in V_{oc} improvement can be explained by the higher bandgap in the SCR. On the other hand, the reduction of the spike from 0.28 eV from the pure selenium to 0.15 eV to the one with sulfur in the interface can explain the increase of 6 points in the FF and the relatively low decrease of the J_{sc} for the sulfur-rich cell, mainly due to the decreased recombination at the CIGSSe/CdS interface.

4.2.2 Drift diffusion models for organic solar cells

When we are dealing with the electrical modeling of OSCs, we have to take into account the presence of excitons and the disordered character of the active layer. Absorption of photons essentially occurs in the donor material and leads to the generation of bounded charges called excitons. An exciton has to diffuse until it reaches a donor/acceptor interface to allow an electron to be transferred to an acceptor molecule. Thus, at this interface, a so-called charge transfer exciton (CT-exciton) is generated. In a CT-exciton, even if the two charges are located on different molecules, the hole and the electron are still bound by a Coulombic binding which should be broken to generate free charges. The CT-exciton can then diffuse at the interface within a distance of a few nanometers before recombining or being dissociated into free charges or being lost at one electrode.[87,88] The physical processes that govern the charge generation and the charge transportation in OSCs can be modeled at the molecular scale[88,89] or at a macroscopic scale using a drift diffusion model.[90] In the following, we will focus on drift diffusion models.

Figure 21(a) presents the block diagram of the process used by Häusermann et al.[91] for exciton modeling in 1D within P3HT:PCBM-based OSCs. In this model, the authors assumed that a CT-exciton is directly generated after the absorption of one photon. $G_{opt}(x)$ stands for the position-dependent generation rate while g_{eff} is the photon-to-CT-exciton conversion efficiency. g_{eff} has been used as a fitting parameter by Häusermann et al.[91] Following the model proposed by Koster et al.,[90] the active layer is considered to be an effective homogeneous layer. Because the semiconducting materials are not doped in usual OSCs, the active layer is considered to be an intrinsic semiconductor exhibiting a bandgap equal to the difference between the LUMO of the acceptor material and the HOMO of the donor material.[90] The CT-exciton can be separated into free charges with a rate constant k_d or recombined with a rate constant k_f, $S(x)$ being the position-dependent CT-exciton density. For the CT-exciton dissociation, an Onsager–Braun model[92,93] was used in which the dissociation process results from a competition between a bimolecular recombination of Langevin and an electric field–dependent dissociation process. Two free charges can also recombine into a CT-exciton through the bimolecular recombination process of Langevin with a rate $r_{eff}r(x)$, where $r(x)$ is

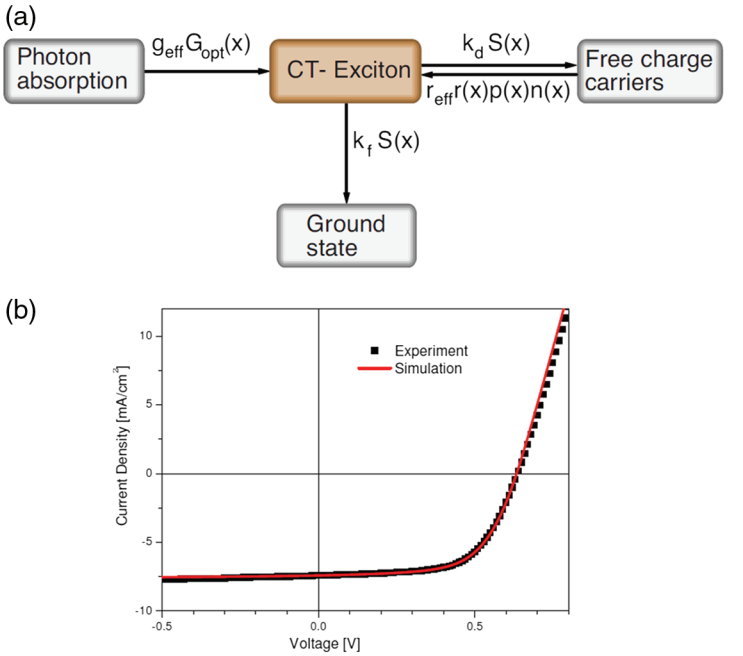

Figure 21 (a) Block diagram of the process for CT-exciton modeling used by Häusermann et al. (extracted from Ref. 86) and (b) comparison between a simulated and an experimentally measured *I*(*V*) characteristic for a P3HT:PCBM-based solar (extracted from Ref. 91).

the position-dependent bimolecular recombination of Langevin [see Eq. (22)] and r_{eff} is a factor between 0 and 1 representing the recombination efficiency through a recombination process of Langevin. It has been used as a fitting parameter by Häusermann et al.[91] The following drift diffusion model was implemented

$$\frac{dE(x)}{dx} = \frac{e}{\varepsilon_r \varepsilon_0}[p(x) - n(x)], \tag{21}$$

$$\frac{dS(x)}{dt} = r_{\text{eff}} r(x) p(x) n(x) - k_{\text{f}} S(x) - k_{\text{d}} S(x) + g_{\text{opt}}(x), \tag{22}$$

$$J_{\text{e}}(x) = e\mu_{\text{e}} n(x) E(x) + D(\mu, T)\frac{\text{d}n(x)}{\text{d}x}, \tag{23}$$

$$\frac{dn(x)}{dt} = \frac{1}{e}\frac{dJ_{\text{e}}(x)}{dx} - r_{\text{eff}} r(x) p(x) n(x) + k_{\text{d}} S(x), \tag{24}$$

where $n(x)$, $p(x)$ and $S(x)$ are the position-dependent electron, hole, and CT-exciton densities; $G_{\text{opt}}(\text{x})$ is the position-dependent generation rate; μ_{e} is the electron mobility and $D(\mu, T)$ the diffusion coefficient given by the Einstein

relation; $r(x) = (\mu_e + \mu_p)e/(\varepsilon_r\ \varepsilon_0)$ is the bimolecular recombination of Langevin; and e and T are the charge of the electron and the temperature, respectively.

Equation (21) is the Poisson equation. Equation (22) is the continuity equation corresponding to the CT-exciton while Eqs. (23) and (24) are the current equation and the continuity equation, respectively, for the electrons. In this model, expressions analog to the (23) and (24) expressions were used for the holes. $G_{opt}(x)$ is the position-dependent generation rate and was calculated using a TMM. For nonplanar solar cells, 2D optical modeling of the generation rate using an FE method, an RCWA method, or an FDTD method followed by 2D resolutions of the drift diffusion model, can be implemented.[73,74,94,95] Figure 21(b) shows a comparison between simulated and experimentally measured I(V) characteristics for a P3HT:PCBM-based solar cell.[91] The very good agreement between experimental measurements and 1D numerical modeling shows that such a model is reliable even if based on strong assumptions.

Figure 22 shows results concerning the three-dimensional resolution of exciton-diffusion equations in P3HT:ZnO-based hybrid organic/inorganic solar cells. The aim was to correlate the cell performances with the three-dimensional

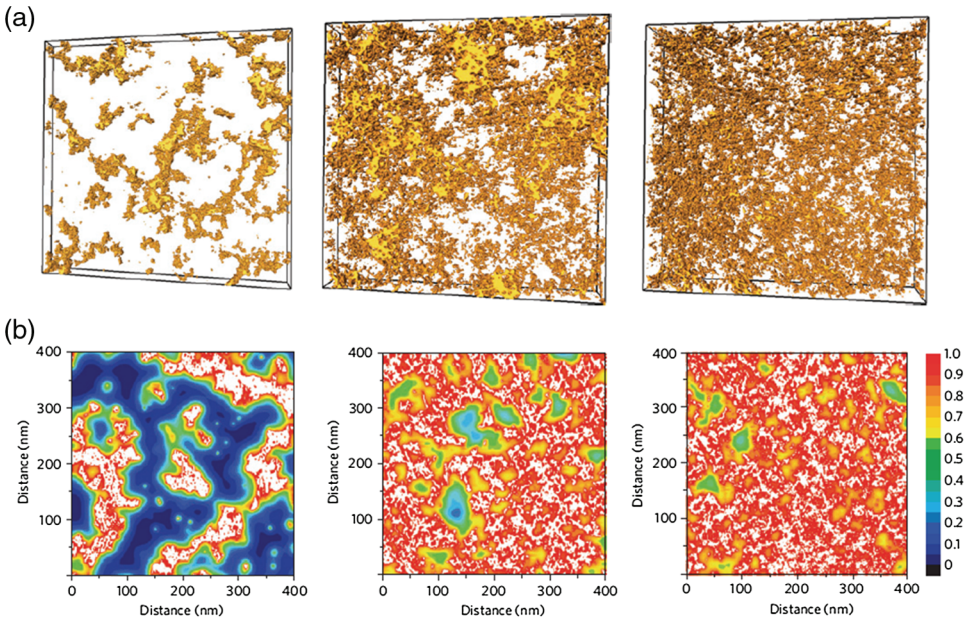

Figure 22 (a) Reconstructed volume of active layers in P3HT:ZnO obtained by electron tomography for three different thicknesses: (left) 57 nm, (center) 100 nm, and (right) 167 nm (extracted from Ref. 96) and (b) calculated quenching efficiency cross sections in the bulk material for three different active layer thicknesses: (left) 57 nm, (center) 100 nm, and (right) 167 nm (source: extracted from Ref. 96). ZnO appears in yellow and P3HT appears transparent.

morphology of the active layer.[96] Figure 22(a) shows reconstructed volumes of active layers in P3HT:ZnO obtained by electron tomography. ZnO appears in yellow while P3HT appears transparent. The three images correspond to three different active layer thicknesses [57 nm (left), 100 nm (center), and 167 nm (right)]. These images clearly prove that the phase separation depends on the P3HT:ZnO-based active layer thickness: the size of the material domain decreases with increasing thickness. The authors modeled the exciton diffusion inside the active layer by solving the following diffusion equation in 3D:

$$\frac{dX}{dt} = -\frac{X}{\tau} + D\nabla^2 X + g, \tag{25}$$

where D is the diffusion constant, X is the exciton density, τ is the exciton lifetime, and g is the exciton generation rate. Figure 22(b) shows the calculated exciton quenching efficiency cross sections in the bulk material for the three above-mentioned active layer thicknesses. Absorption of photons mainly occurs in the donor material (P3HT) and results in the generation of excitons. The exciton quenching inside the active layer corresponds to the electron transfer from P3HT to ZnO and results in the dissociation of the excitons. Figure 22(b) gives color maps of the exciton quenching efficiency inside the active layer for three different thicknesses. These results reveal an improved quenching efficiency for thick layers due to the presence of smaller material domains. Indeed, due to much finer morphology, excitons are generated closer to ZnO in thick active layers than in thin active layers, which results in a better dissociation of the excitons in thick layers than in thin layers.

5 Conclusion

Through several examples, we point out the necessity to have precise modeling and precise measurements in order to predict the optical properties of thin-film solar cells. The materials used nowadays in these cells are quite complex, present high absorption but also some defects. Thus, it is quite difficult to predict the optoelectronic behavior of these new devices involving a strong link between optics (absorption of the light) and electronics (collection of the electrons). There is a large set of optical techniques that provide insight into the optoelectronic phenomena that occur in thin-film-layer-based solar cells. Among these powerful tools, we propose to use ellipsometry, spectrophotometry, PL, and PR characterizations that can be combined in order to precisely define some of important parameters of a material (electronic levels, n and k). However, without complete modeling of our cells, we cannot conclude nor predict their performances. The physics of the materials must be implemented in order to have a complete model of our device. Improving the performance of solar cells requires a thorough knowledge of the optical properties of the different layers, and this knowledge is acquired through the joint use of very precise optical measurements and a comprehensive optoelectrical model.

References

1. A. Polman and H. A. Atwater, "Photonic design principles for ultrahigh-efficiency photovoltaics," *Nat. Mater.* **11**, 174–177 (2012).
2. P. Bermel et al., "Improving thin-film crystalline silicon solar cell efficiencies with photonic crystals," *Opt. Express* **15**, 16986–17000 (2007).
3. M. Niggemann et al., "Diffraction gratings and buried nano-electrodes—architectures for organic solar cells," *Thin Solid Films* **451–452**, 619–623 (2004).
4. M. Notarianni et al., "Plasmonic effect of gold nanoparticles in organic solar cells," *Solar Energy* **106**, 23–37 (2014).
5. D. Duche et al., "Photonic crystals for improving light absorption in organic solar cells," *J. Appl. Phys.* **117**(5), 053108 (2015).
6. H. Sai et al., "Triple-junction thin-film silicon solar cell fabricated on periodically textured substrate with a stabilized efficiency of 13.6%," *Appl. Phys. Lett.* **106**, 213902 (2015).
7. M. A. Green et al., "Solar cell efficiency tables (version 46)," *Prog. Photovoltaics Res. Appl.* **23**, 805–812 (2015).
8. W. Wang et al., "Device characteristics of CZTSSe thin-film solar cells with 12.6% efficiency," *Adv. Energy Mater.* **4**, 1301465 (2014).
9. W. Shockley and H. J. Queisser, "Detailed balance limit of efficiency of pn junction solar cells," *J. Appl. Phys.* **32**, 510 (1961).
10. L. Kranz et al., "Doping of polycrystalline CdTe for high-efficiency solar cells on flexible metal foil," *Nat. Commun.* **4**, 2306 (2013).
11. J. D. Chen et al., "Single-junction polymer solar cells exceeding 10% power conversion efficiency," *Adv. Mater.* **27**(6), 1035–1041 (2015).
12. Z. He et al., "Single-junction polymer solar cells with high efficiency and photovoltage," *Nat. Photonics* **9**, 174–179 (2015).
13. J. You et al., "A polymer tandem solar cell with 10.6% power conversion efficiency," *Nat. Commun.* **4**, 1446 (2012).
14. J. Maçaira, L. Andrade, and A. Mendes, "Review on nanostructured photoelectrodes for next generation dye-sensitized solar cells," *Renew. Sustainable Energy Rev.* **27**, 334–349 (2013).
15. H. J. Snaith, "Perovskites: the emergence of a new era for low-cost, high efficiency solar cells," *J. Phys. Chem. Lett.* **4**(21), 3623–3630 (2013).
16. N. Park, "Organometal perovskite light absorbers toward a 20% efficiency low-cost solid-state mesoscopic solar cell," *J. Phys. Chem. Lett.* **4**, 2423–2439 (2013).
17. H. J. Snaith, "Estimating the maximum attainable efficiency in dye-sensitized solar cells," *Adv. Funct. Matter.* **19**, 1–7 (2010).
18. H. Zhou et al., "Interface engineering of highly efficient perovskite solar cells," *Science* **345**, 542 (2014).
19. M. Liu, M. B. Johnston, and H. J. Snaith, "Efficient planar heterojunction perovskite solar cells by vapour deposition," *Nature* **501**(7467), 395–398 (2013).
20. W. A. Laban and L. Etgar, "Depleted hole conductor-free lead halide iodide heterojunction solar cells," *Energy Environ. Sci.* **6**, 3249–3253 (2013).
21. M. A. Green et al., "The emergence of perovskite solar cells," *Nat. Photonics* **8**, 506–514 (2014).
22. A. Kojima et al., "Organometal halide perovskites as visible-light sensitizers for photovoltaic cells," *J. Am. Chem. Soc.* **131**(17), 6050–6051 (2009).
23. G. E. Eperon et al., "Neutral color semitransparent microstructured perovskite solar cells," *ACS Nano* **8**(1), 591–598 (2014).
24. C. Roldan et al., "High efficiency single-junction semitransparent perovskite solar cells," *Energy Environ. Sci.* **7**, 2968 (2014).

25. W. Nie et al., "High-efficiency solution-processed perovskite solar cells with millimeter-scale grains," **347**(6221), 522–525 (2015).
26. V. D'Innocenzo et al., "Excitons versus free charges in organo-lead tri-halide perovskites," *Nat. Commun.* **5**, 3586 (2014).
27. S. D. Stranks et al., "Electron–hole diffusion lengths exceeding 1 micrometer in an organometal trihalide perovskite absorber," *Science* **342**, 341–344 (2013).
28. M. A. Loi and J. C. Hummelen, "Perovskites under the sun," *Nat. Mater.* **12**, 1087–1089 (2013).
29. J. Bisquert, "The swift surge of perovskite photovoltaics," *J. Phys. Chem. Lett.* **4**, 2597–2598 (2013).
30. T. Kirchartz, K. Ding, and U. Rau, "Fundamental electrical characterization of thin-film solar cells," in *Advanced Characterization Techniques for Thin Film Solar Cells*, D. Abou-Ras, T. Kirchartz, and U. Rau, Editors, pp. 35–60, Wiley-VCH Verlag GmbH & Co. KGaA: Weinheim, Germany (2011).
31. S. S. Hegedus and W. N. Shafarman, "Thin-film solar cells: device measurements and analysis," *Prog. Photovoltaics Res. Appl.* **12**(23), 155–176 (2004).
32. S. Siebentritt, "What limits the efficiency of chalcopyrite solar cells?" *Sol. Energy Mater. Sol. Cells* **95**(6), 1471–1476 (2011).
33. P. Jackson et al., "Properties of Cu(In, Ga)Se_2 solar cells with new record efficiencies up to 21.7%," *Phys. Status Solidi Rapid Res. Lett.* **9**(1), 28–31 (2015).
34. G. Sozzi, F. Troni, and R. Menozzi, "On the combined effects of window/buffer and buffer/absorber conduction-band offsets, buffer thickness and doping on thin-film solar cell performance," *Sol. Energy Mater. Sol. Cells* **121**(2014), 126–136 (2014).
35. P. D. Paulson, R. W. Birkmire, and W. N. Shafarman, "Optical characterization of $CuIn_{1-x}Ga_xSe_2$ alloy thin films by spectroscopic ellipsometry," *J. Appl. Phys.* **94**(2), 879–888 (2003).
36. K. T. Cheung et al., "Towards FDTD modeling of spectroscopic ellipsometry data at large angles of incidence," *Appl. Surf. Sci.* **281**, 2–7 (2013).
37. A. Keeman et al., "Optical response of silver nanoneedles on a mirror," *Plasmonics* **10**(5), 1089–1096 (2015).
38. H. El Rhaleb et al., "Spectroscopic ellipsometry studies of index profile of indium tin oxide films prepared by spray pyrolysis," *Appl. Surf. Sci.* **201**, 138–145 (2002).
39. A. D. Rakic et al., "Optical properties of metallic films for vertical-cavity optoelectronic devices," *Appl. Opt.* **37**(22), 5271–5283 (1998).
40. G. E. Jellison and F. A. Modine, "Parameterization of the optical functions of amorphous materials in the interband region," *Appl. Phys. Lett.* **69**, 371 (1996).
41. D Duché et al., "Optical performance and color investigations of hybrid solar cells based on P3HT:ZnO, PCPDTBT:ZnO, PTB7:ZnO and DTS$(PTTh_2)_2$:ZnO," *Sol. Energy Mater. Sol. Cells* **126**, 197–204 (2014).
42. F. Bencheikh-Aboura et al., "Ellipsometric study of the optical transitions of $PC_{60}BM$ and $PC_{70}BM$ thin films," *Chem. Phys.* **450–451**, 102–108 (2015).
43. B. Han et al., "Electronic transitions and excitations in solid C_{70} studied by reflection electron energy loss spectroscopy," *J. Vac. Surf. Films* **13**(3), 1606–1608 (1995).
44. H. Ajie, M. Alvarez, and S. Anz, "Characterization of the soluble all-carbon molecules C_{60} and C_{70}," *J. Phys. Chem.* **94**, 8630–8633 (1990).
45. A. Nakamura et al., "Ultrafast relaxation of excitons and photopolymerization in C_{60} and C_{70}," *J. Lumin.* **66–67**(95), 383–388 (1995).
46. T. Unold and L. Gütay, "Photoluminescence analysis of thin-film solar cells," in *Advanced Characterization Techniques for Thin Film Solar Cells*, D. Abou-Ras, T. Kirchartz, and U. Rau, Editors, pp. 151–175, Wiley-VCH Ver lag GmbH & Co. KGaA., Weinheim, Germany (2011).

47. T. Schmidt, K. Lischka, and W. Zulehner, "Excitation power dependence of the near-band-gap-edge photoluminescence of semiconductors," *Phys. Rev. B* **45**(16), 45–50 (1992).
48. J. Krustok, H. Collan, and K. Hjelt, "Does the low-temperature Arrhenius plot of the photoluminescence intensity in CdTe point towards an erroneous activation energy?" *J. Appl. Phys.* **81**(3), 1442–1445 (1997).
49. F. Bencheikh et al., "Study of optical properties and molecular aggregation of conjugated low band gap copolymers: PTB7 and PTB7-Th," *J. Phys. Chem. C* **119**(43), 24643–24648 (2015).
50. E. Menéndez-Proupin et al., "Self-consistent relativistic band structure of the $CH_3NH_3PbI_3$ perovskite," *Phys. Rev. B* **90**, 045207 (2014).
51. C. M. Ruiz et al., "Using combined photoreflectance and photoluminescence for understanding optical transitions in perovskites," in *42th IEEE Photovoltaic Specialists Conf. (PVSC)* (2015).
52. C. M. Sutter-Fella et al., "High photoluminescence quantum yield in band gap tunable bromide containing mixed halide perovskites," *Nano Lett.* **16**, 800–806 (2015).
53. A. Miyata et al., "Direct measurement of the exciton binding energy and effective masses for charge carriers in organic–inorganic tri-halide perovskites," *Nat. Phys.* **11**, 582–587 (2015).
54. E. R. Dohner et al., "Self-assembly of broadband white-light emitters," *JACS Commun.* **136**, 1718 (2014).
55. P. W. Yu, "Excitation-dependentemission in Mg-, Be-, Cd-, and Zn-implanted GaAs," *J. Appl. Phys.* **48**, 5043 (1977).
56. J. Krustok et al., "The role of spatial potential fluctuations in the shape of the PL bands of multinary semiconductor compounds," *Phys. Scr.* **T79**(1), 179 (1999).
57. C. M. Ruiz, "Modification of optoelectronical properties of CdTe based solar cells by Bismuth doping," PhD Thesis, Universidad Autónoma de Madrid, Spain (2007).
58. D. E. Aspnes, "Band nonparabolicities, broadening, and internal field distributions: the spectroscopy of Franz–Keldysh oscillations," *Phys. Rev. B* **10**(10), 4228–4240 (1974).
59. A. Hamnett, J. Gilman, and R. A. Batchelor, "Theory of electroreflectance and photoreflectance of semiconductors," *Electrochim. Acta* **37**(5), 949–956 (1992).
60. J. Misiewicz et al., "Photomodulated reflectance and transmittance: optical characterisation of novel semiconductor materials and device structures," *Thin Solid Films* **450**(1), 14–22 (2004).
61. J. Eberhardt et al., "Excitonic luminescence of polycrystalline $CuInS_2$ solar cell material under the influence of strain," *J. Appl. Phys.* **102**(3), 033503 (2007).
62. A. Moreau et al., "Understanding CIGS device performances through photoreflectance spectroscopy," *Proc. SPIE* **8470**, 7 (2012).
63. A. Moreau et al., "Impact of Cu–Au type domains in high current density $CuInS_2$ solar cells," *Sol. Energy Mater. Sol. Cells* **139**, 101–107 (2015).
64. M. I. Alonso et al., "Optical functions and electronic structure of $CuInSe_2$, $CuGaSe_2$, $CuInS_2$, $CuGaS_2$," *Phys. Rev. B* **63**(7), 075203 (2001).
65. T. Leijtens et al., "Stability of metal halide perovskite solar cells," *Adv. Energy Mater.* **5**(20), 1500963 (2015).
66. National Renewable Energy Laboratory, (NREL), "Renewable Resource Data Center," (last revision 2012). http://rredc.nrel.gov/solar/spectra.
67. L. A. A. Pettersson, L. S. Roman, and O. Inganäs, "Modeling photocurrent action spectra of photovoltaic devices based on organic thin films," *J. Appl. Phys.* **86**, 487 (1999).
68. S. Ben Dkhil et al., "Interplay of optical spacer, morphological and electronic effects of ZnO interlayers in polymer solar cells using regular device structures," *Adv. Energy Mater.* **4**, 1400805 (2014).
69. M. Gaceur et al., "Ligand-free synthesis of aluminum-doped zinc oxide nanocrystals and their use as optical spacers in color tuned high-efficient organic solar cells," *Adv. Func. Energy* **26**, 243–253 (2015).

70. I. Massiot et al., "Metal nanogrid for broadband multiresonant light-harvesting in ultrathin GaAs layers," *ACS Photonics* **1**, 878–884 (2014).
71. D. Duche et al., "Improving light absorption in organic solar cells by plasmonic contribution," *Sol. Energy Mater. Sol. Cells* **93**, 1377–1382 (2009).
72. S. Vedraine et al., "Intrinsic absorption of plasmonic structures for organic solar cells," *Sol. Energy Mater. Sol. Cells* **95**, S57–S64 (2011).
73. W. Vervisch et al., "Optical–electrical simulation of organic solar cells: influence of light trapping by photonic crystal and ZnO spacer on electrical characteristics," *J. Appl. Phys.* **111**, 094506 (2012).
74. W. Vervisch et al., "Optical–electrical simulation of organic solar cells: excitonic modeling parameter influence on electrical characteristics," *Appl. Phys. Lett.* **98**, 253306 (2011).
75. D. Duché et al., "Light harvesting in organic solar cells," *Sol. Energy Mater. Sol. Cells* **95**, S18–S25 (2011).
76. D. Duché et al., "Slow bloch modes for enhancing the absorption of light in thin films for photovoltaic cells," *Appl. Phys. Lett.* **92**, 193310 (2008).
77. B. E. Pieters et al., "One-dimensional electro-optical simulations of thin-film solar cells," in *Advanced Characterization Techniques for Thin Film Solar Cells*, pp. 501–527, Wiley-VCH Verlag GmbH & Co. KGaA., Weinheim, Germany (2011).
78. S. M. Sze, *Semiconductor Devices: Physics and Technology*, John Wiley & Sons, New York (2008).
79. A. Pudov et al., "CIGS J–V distortion in the absence of blue photons," *Thin Solid Films* **480–481**, 273–278 (2005).
80. A. Pudov et al., "Secondary barriers in CdS–$CuIn_{1-x}Ga_xSe_2$ solar cells," *J. Appl. Phys.* **97**(6), 064901 (2005).
81. C. Insignares-Cuello et al., "Advanced characterization of electrodeposition-based high efficiency solar cells: non-destructive Raman scattering quantitative assessment of the anion chemical composition in $Cu(In,Ga)(S,Se)_2$ absorbers," *Sol. Energy Mater. Sol. Cells* **143**, 212–217 (2015).
82. M. Burgelman, P. Nollet, and S. Degrave, "Modelling polycrystalline semiconductor solar cells," *Thin Solid Films* **361–362**(1–2), 527–532 (2000).
83. I. L. Repins et al., "19.9%-efficient ZnO/CdS/$CuInGaSe_2$ solar cell with 81.2% fill factor," *Prog. Photovoltaics Res. Appl.* **16**, 235–239 (2008).
84. B. J. Mueller et al., "Influence of different sulfur to selenium ratios on the structural and electronic properties of $Cu(In,Ga)(S,Se)_2$ thin films and solar cells formed by the stacked elemental layer process," *J. Appl. Phys.* **116**(17), 174503 (2014).
85. Y. Goushi et al., "Fabrication of pentanary $Cu(InGa)(SeS)_2$ absorbers by selenization and sulfurization," *Sol. Energy Mater. Sol. Cells* **93**(8), 1318–1320 (2009).
86. M. Burgelman and J. Marlein, "Analysis of graded band gap solar cells with SCAPS," in *23rd European Photovoltaic Solar Energy Conf. and Exhibition (September)*, pp. 1–5 (2008).
87. T. Strobel, C. Deibel, and V. Dyakonov, "Role of polaron pair diffusion and surface losses in organic semiconductor devices," *Phys. Rev. Lett.* **105**, 266602 (2010).
88. T. Strobel and V. Dyakonov, "Role of the charge transfer state in organic donor–acceptor solar cells," *Adv. Mater.* **22**(37), 4097–4111 (2010).
89. S. Athanasopoulos et al., "Predictive study of charge transport in disordered semiconducting polymers," *Nano Lett.* **7**(6), 1785–1788 (2007).
90. L. J. A. Koster et al., "Device model for the operation of polymer/fullerene bulk heterojunction solar cells," *Phys. Rev. B* **72**, 085205 (2005).
91. R. Häusermann et al., "Coupled opto-electronic simulation of organic bulk-heterojunction solar cells: parameter extraction and sensitivity analysis," *J. Appl. Phys.* **106**, 104507 (2009).
92. L. Onsager, "Initial recombination of ions," *Phys. Rev.* **54**, 554 (1938).

93. C. L. Braun, "Electric field assisted dissociation of charge transfer states as a mechanism of photocarrier production," *J. Chem. Phys.* **80**, 4157 (1984).
94. F. F. Stelzl and U. Wurfel, "Modeling the influence of doping on the performance of bulk heterojunction organic solar cells: one-dimensional effective semiconductor versus two-dimensional donor/acceptor model," *Phys. Rev. B* **86**, 75315 (2012).
95. C. Kirsch and S. Mitran, "Simulated annealing electro-photonic optimization of organic solar cells," *J. Appl. Phys.* **112**, 054502 (2012).
96. S. D. Oosterhout et al., "The effect of three-dimensional morphology on the efficiency of hybrid polymer solar cells," *Nat. Mater.* **8**, 818–824 (2009).

Carmen M. Ruiz graduated in Physics in 2001 and obtained her Ph.D. in Applied Physics in 2007 at the Universidad Autónoma de Madrid. Since then, she has been working both in academia and industry. In 2012, she transferred to Aix-Marseille University, France, where she works in optical and electrical characterization of photovoltaic materials and cells, the focus of her research career. She is the author or co-author of 42 publications.

David Duché is a researcher at the IM2NP laboratory. He obtained his Ph.D. from Aix-Marseille University in 2010 for his work on photonic structures for organic solar cells (modeling and experiments). He has worked on several research projects, centered primarily on new photonics concepts for light harvesting. He develops numerical models to optimize solar cell performance and has a strong expertise in optical characterization, such as ellipsometry. He is the author or co-author of 25 publications.

Judikaël Le Rouzo is presently an Associate Professor of Physics at Aix-Marseille University. He received his Ph.D. in Physics from the Ecole Polytechnique, France. His research at the IM2NP CNRS laboratory centers mainly on optoelectronic devices, such as photodetectors and photovoltaic solar cells. He specializes in optics and photonics, especially thin films and nanostructure layers. He is the author or co-author of more than 45 publications.